This manuscript represents a post-print that has been accepted in the *Journal of Petrology* following peer-review (submitted 24th of August 2020).

# Upper mantle mush zones beneath low melt flux ocean island volcanoes: insights from Isla Floreana, Galápagos

Matthew L. M. Gleeson[1,2]*, Sally A. Gibson[1] and Michael J. Stock[1,3]
[1]Department of Earth Sciences, University of Cambridge, Downing Street, CB2 3EQ, UK
[2]School of Earth and Ocean Sciences, Cardiff University, Park Place, Cardiff, CF10 3AT, UK
[3]Department of Geology, Trinity College Dublin, College Green, Dublin 2, Ireland.
*Corresponding author email address: matthew.gleeson.geo@gmail.com

## ABSTRACT

The physicochemical characteristics of sub-volcanic magma storage regions have important implications for magma system dynamics and pre-eruptive behaviour. The architecture of magma storage regions located directly above high buoyancy flux mantle plumes (such as Kīlauea, Hawai'i and Fernandina, Galápagos) are relatively well understood. However, far fewer constraints exist on the nature of magma storage beneath ocean island volcanoes that are distal to the main zone of mantle upwelling or above low buoyancy flux plumes, despite these systems representing a substantial proportion of ocean island volcanism globally. To address this, we present a detailed petrological study of Isla Floreana in the Galápagos Archipelago, which lies at the periphery of the upwelling mantle plume and is thus characterised by an extremely low flux of magma into the lithosphere. Detailed *in situ* major and trace element analyses of crystal phases within exhumed cumulate xenoliths, lavas and scoria deposits, indicate that the erupted crystal cargo is dominated by disaggregated crystal-rich material (i.e., mush or wall rock). Trace element disequilibria between cumulus phases and erupted melts, as well as trace element zoning within the xenolithic clinopyroxenes, reveals that reactive porous flow (previously identified beneath mid-ocean ridges) is an important process of melt transport within crystal-rich magma storage regions. In addition, application of three petrological barometers reveal that the Floreana mush zones are located in the upper mantle, at a depth of 23.7±5.1 km. Our barometric results are compared to recent studies of high melt flux volcanoes in the western Galápagos, and other ocean island volcanoes worldwide, and

demonstrate that the flux of magma from the underlying mantle source represents a first-order control on the depth and physical characteristics of magma storage.


## KEY WORDS

Galápagos; magma storage; reactive porous flow; barometry.


# 1 INTRODUCTION

The physicochemical characteristics (such as size, pressure, volatile content and geochemical heterogeneity) of magma storage at volcanic centres located directly above high buoyancy flux mantle plumes (e.g. Kīlauea, Hawai'i and Isabela, Galápagos) have been subject to intense study over the past few decades (Bagnardi et al., 2013; Bernard et al., 2019; Clague and Denlinger, 1994; Geist et al., 1998; Naumann and Geist, 1999; Neal et al., 2019; Park et al., 2007; Pietruszka et al., 2015; Poland et al., 2015; Sides et al., 2014; Stock et al., 2018; Wieser et al., 2020, 2019). Systems such as Kīlauea are characterised by frequent volcanic activity, and geophysical (seismicity, ground deformation) and geochemical (gas emissions) monitoring is prevalent. Monitoring data, combined with petrological and geochemical analysis of erupted products (mineral textures, deformation characteristics and chemistry) provide important insights into the architecture and dynamics of their sub-volcanic plumbing systems (Amelung et al., 2000; Davidge et al., 2017; Geist et al., 2014; Hartley et al., 2018; McCormick Kilbride et al., 2016). However, these systems (which we term 'high melt flux') represent only one endmember of global plume-derived volcanism. Low melt flux systems, either above low buoyancy flux plumes (e.g. Canary Islands; Longpre et al., 2014) or at volcanic systems distal to the centre of mantle melting at high buoyancy flux mantle plumes (e.g. eastern and south-eastern Galápagos; Harpp and Geist, 2018), are the other endmember.

While a substantial number of hotspot-related volcanic systems that have been active during the Holocene are located in regions characterised by a relatively low flux of magma into the lithosphere (i.e., regions distal to the main zone of plume upwelling or above low buoyancy flux plumes; Samoa, Canary Islands, Cape Verde; Global Volcanism Program, 2013), only a small number of eruptions have been observed (and recorded) at these systems since the advent of modern volcano monitoring

techniques. As a result, few constraints exist on the conditions of magma storage in regions characterised by a low flux of magma into the lithosphere, relative to volcanic centres located above the centre of mantle plumes with a large buoyancy flux (and thus generating a large flux of magma and more frequent eruptions).

The flux of mantle-derived magma into the lithosphere is thought to impart a first-order control on the evolution of ocean island volcanoes and the homogeneity of erupted liquids (Geist et al., 2014). Therefore, placing constraints on the physicochemical characteristics of magma storage at low melt flux ocean island volcanoes is essential for determining the influence of mantle dynamics and melt generation processes on the structure and physical characteristics of sub-volcanic magma plumbing systems. In the absence of detailed monitoring data, petrological and geochemical analyses of volcanic products from past eruptions represent the only available tools for determining the structure and processes operating within these systems, as well as possible eruption precursors.

Isla Floreana in the south-eastern Galápagos is currently located ~100 km downstream from where the centre of the Galápagos plume impacts on the base of the lithosphere beneath the island of Isabela in the western archipelago (Fig. 1; Villagómez et al., 2014). Hence, although the Galápagos plume has a relatively high buoyancy flux compared to regions such as the Canary Islands (Jackson et al., 2017), Floreana's location relative to the main zone of mantle plume upwelling results in an extremely low flux of magma entering the lithosphere and, consequently, very infrequent volcanic activity (Harpp et al., 2014a; Harpp and Geist, 2018). Floreana is considered to be an infrequently active volcanic centre, rather than extinct, owing to the persistent volcanic activity since ~1 Ma and the long-lived nature of volcanism on the eastern Galapagos islands that lie >100 km 'downstream' of the Galapagos mantle plume (e.g. the youngest lavas on San Cristobal are ~9 ka; Mahr et al., 2016).

In this paper, we present a thorough petrological study of scoria, lava and xenolith samples from Floreana and place constraints of the structure, depth and crystallinity of magmatic systems beneath this low melt flux ocean island volcano. We compare our results with more frequently active volcanic centres in the western Galápagos (near the centre of plume upwelling; Geist et al., 1998; Naumann and Geist, 1999; Stock et al., 2018), as well as other ocean island volcanoes worldwide (Hammer et

al., 2016; Hartley et al., 2018; Poland et al., 2015), to investigate how the flux of magma into the lithosphere influences the depth and crystallinity of sub-volcanic magma storage regions.

# 2 GEOLOGICAL BACKGROUND

The Galápagos Archipelago in the eastern equatorial Pacific is one of the most volcanically active regions on Earth, with eruptions typically occurring every 2–3 years (Global Volcanism Program, 2013). Although most historic Galápagos eruptions have taken place on the two westernmost islands of Isabela and Fernandina (Fig. 1), infrequent volcanic activity has also occurred on several islands in the eastern and south-eastern Galápagos (for example, Santiago in 1906 and Marchena in 1991; Global Volcanism Program, 2013). In fact, volcanic activity in the eastern Galapagos, >100 km 'downstream' of the postulated position of the plume stem, has been shown to be long-lived, with volcanic activity on San Cristobal extending over 2 Myrs with the most recent lavas erupted at ~9 ka (Mahr et al., 2016).

Volcanoes in the western Galápagos likely emerged within the last 500 kyr (Naumann and Geist, 2000), whereas those in the eastern and south-eastern Galápagos are considerably older (eruption ages up to 2.3 Ma and 3.2 Ma have been measured on San Cristobal and Espanola, respectively; Bailey, 1976; Geist et al., 1986). In addition, substantial differences in geomorphology and the style of volcanic activity are observed across the archipelago (Geist et al., 1995; Harpp et al., 2014a; Harpp and Geist, 2018). For example, volcanoes in the western archipelago are typified by large summit calderas (<700m deep), which are not present on the eastern islands (Chadwick and Howard, 1991; Cleary et al., 2020; Harpp and Geist, 2018).

Geochemical distinctions between the western and eastern/south-eastern Galápagos islands are also observed, which are primarily related to variations in the composition of the underlying mantle source (Geist et al., 1988; Gibson and Geist, 2010; Gleeson et al., 2020; Harpp and White, 2001; White et al., 1993) or the volume flux of mantle-derived magma that ascends into the lithosphere (Geist et al., 1995, 2014; Gibson et al., 2016; Harpp and Geist, 2018). For example, variations in the flux of mantle derived magma are hypothesised to influence the geochemical heterogeneity of erupted basalts at each

island: volcanoes in the western archipelago typically erupt a very narrow range of basaltic compositions over hundreds of millennia during their main shield building phase, whereas basalts erupted from a single island in the eastern and/or south-eastern archipelago, such as Floreana, tend to display far greater compositional heterogeneity (Geist et al., 2014; Harpp and Geist, 2018).

Floreana is characterised by numerous scoria cones and blocky, heavily vegetated lava flows that can typically be traced to the cone from which they originated (Bow and Geist, 1992; Harpp et al., 2014a). The crustal thickness beneath Floreana is ~16 km, similar to that observed in the western Galápagos 10–18 km (Feighner and Richards, 1994), and the lithospheric thickness beneath the western and south-eastern Galápagos is very similar (~50–60 km; Gibson and Geist, 2010). Recent work has shown that the average volumetric eruption rate on Floreana over the past 1–1.5 Myrs is 1–10 $m^3 \cdot yr^{-1}$, 6 orders of magnitude lower than the current volcanic productivity at volcanoes in the western Galápagos (cf. ~$4.4 \cdot 10^6$ $m^3 \cdot yr^{-1}$ at Fernandina; Harpp et al., 2014a; Kurz et al., 2014). This difference in volumetric eruption rate likely reflects a substantially lower flux of magma into the lithosphere beneath Floreana than beneath each volcanic centre in the western Galápagos.

Despite the relatively low volcanic productivity of Floreana over the last ~1–1.5 Myrs, the erupted products have several important characteristics that provide insights into the nature of the underlying magmatic system. For example, Floreana has a high proportion of pyroclastic deposits compared to the other Galápagos islands (Harpp et al., 2014a) and eruption deposits typically contain a large number of cumulate xenoliths (Bow and Geist, 1992; Lyons et al., 2007), which have been interpreted as evidence for very high magma ascent rates (Harpp et al., 2014a).

Floreana is the only Galápagos island that displays evidence for multiple stages in its volcanic evolution. Submarine parts of the island have isotopic and trace element characteristics that are similar to those measured in recent basalts erupted on southern Isabela, near the centre of plume upwelling (e.g. Sierra Negra and Cerro Azul, Fig. 1A), whereas the subaerial material is isotopically distinct (high $^{206}Pb/^{204}Pb$ and $^{87}Sr/^{86}Sr$ ratios; Harpp et al., 2014). The trace element and isotopic differences between the erupted basalts is mirrored in xenoliths found in the Floreana lava and scoria deposits: gabbroic xenoliths have radiogenic isotope ratios that are similar to modern Isabela basalts,

whereas wehrlitic xenoliths have trace element and isotopic compositions that resemble recent Floreana subaerial basalts (Lyons et al., 2007). Differences in the isotopic characteristics of the Floreana lavas (submarine vs subaerial) and xenoliths (gabbros vs wehrlites) are thought to indicate a change in the mean composition of magma produced by mantle melting beneath the island at ~1–1.5 Ma (Harpp et al., 2014a). In this study, we focus on constraining the depth and physical characteristics of magma storage during the most recent period of volcanic activity on Isla Floreana (<1–1.5 Ma) using chemical and textural analysis of crystal phases in lava flows and xenolithic nodules.

# 3 SAMPLES AND PETROGRAPHY

The Floreana samples analysed in this study consist of lavas (27 samples), scoria (2 samples) and xenoliths (4 wehrlite, 3 dunite and 2 gabbro samples; Fig. 1B). Most lava samples were collected from the unaltered, low vesicularity cores of blocky flows or glassy flow fronts. All samples form part of the Main Series of Floreana lavas identified by Bow and Geist (1992). The scoria samples were collected from two separate deposits and comprise rapidly cooled scoria lapilli (~0.5–2 cm across; 17MMSG16) and bombs (~10 cm across; 17MMSG20). Xenolithic fragments (3–15cm across) were sampled from two different scoria cones on the north-east coast of Floreana; similar xenoliths are also found within most lava flows across the entire island (Supplementary Information).

## 3.1 Lavas and scoria

The lava and scoria samples analysed in this study are typically olivine phyric with minor anhedral clinopyroxene and very rare orthopyroxene. Except for small plagioclase laths in the microcrystalline groundmass, plagioclase crystals are extremely rare in the Floreana lavas. Plagioclase macrocrysts are only present in one of our lava samples (17MMSG29) where they occur as isolated phenocrysts and in plagioclase-olivine crystal clots (Table S.1). The abundance of olivine and absence of plagioclase in the Floreana lavas and scoria contrasts with basalts in the central, northern, and western parts of the Galápagos Archipelago, where plagioclase-phyric and ultraphyric basalts are common (Geist et al., 2002; Gibson et al., 2012; Harpp et al., 2014b).

Despite their relatively simple mineralogy, Floreana lava and scoria samples contain texturally diverse olivine crystals which can be divided into five distinct groups (Fig. 2):

- Group 1 olivines are present in all lava and scoria samples and are the most abundant type of olivine (~60-70% of all crystals). They are characterised by homogeneous cores, with respect to major elements, and narrow normally zoned rims (Fig. 2A). Group 1 olivines are generally subhedral to euhedral.
- Group 2 olivines are the second most abundant group (~20-30%) and display reverse zoning. They are typically euhedral, with occasional small embayments (Fig. 2B).
- Group 3 olivines are also reversely zoned, but are distinguished by skeletal overgrowths, indicating significant undercooling of the host magma and rapid crystal growth (Fig. 2C; Donaldson, 1976; Welsch et al., 2014). Group 3 olivines are less abundant than Groups 1 and 2 olivines (<10%).
- Group 4 olivines are present in low abundance (<10%). They have homogeneous cores and reverse-zoned rims (up to ~300 μm thick). The rims have sieve textures, potentially suggesting resorption and chemical disequilibrium with their carrier melts (Fig. 2D).
- Group 5 olivines are only found in a minority of samples and are characterised by the presence of 4 compositional zones with alternating high and low forsterite contents (visible in back-scattered electron images; Fig. 2E and F).

## 3.2 Xenoliths

### *3.2.1 Gabbroic xenoliths*

Floreana gabbroic xenoliths predominantly comprise plagioclase (33–66 vol.%), clinopyroxene (28–46 vol.%) and orthopyroxene (5–15 vol.%), with little or no olivine (Table S.2). Plagioclase and pyroxene crystals are typically >500 μm and grain sizes are relatively uniform within a single xenolith sample. Where three plagioclase grains meet at a triple junction, 120° grain boundaries indicate a high degree of textural equilibrium (Fig. 3A; Holness et al., 2005). Some of the gabbros have clinopyroxene-rich and plagioclase-rich layers of 2–5 mm thickness.

186 *3.2.2 Dunitic xenoliths*

187 Olivine dominates the dunitic Floreana xenoliths (>90 vol.%). The olivine crystals are subhedral to
188 euhedral and may have undergone partial textural re-equilibration, with some olivine triple junctions
189 approaching 120° grain boundaries. Minor intercumulus clinopyroxene is present along grain
190 boundaries and between pre-existing olivine crystals (Fig. 3B).

191 *3.2.3 Wehrlitic xenoliths*

192 Floreana wehrlitic xenoliths contain olivine (>50 vol.%), clinopyroxene (20–40 vol.%),
193 orthopyroxene (~0–7 vol.%) and minor spinel (<1 vol.%; Table S.2). Clinopyroxene typically occurs
194 as large (<5 mm) oikocrysts, which enclose rounded olivine chadacrysts <500 μm in diameter (Fig.
195 3C and D). Fine-scale orthopyroxene exsolution lamellae (<2 μm) is observed in the clinopyroxenes
196 of a single wehrlite (17MMSG03a; Fig. 3E and F). Olivine grains that are not enclosed by
197 clinopyroxene are typically larger (>1 mm) and more euhedral than the chadacrysts. In some samples,
198 the boundary between clinopyroxene and olivine crystals is characterised by a thin (<20-30 μm) layer
199 of glass and very fine-grained microcrysts. Excluding the rare exsolution lamellae in sample
200 17MMSG03a, orthopyroxene crystals are typically anhedral, infilling the space between earlier
201 formed clinopyroxene and olivine grains. Our observations of dunitic and wehrlitic xenoliths (which
202 have the isotopic signatures of modern day Floreana basalts; Lyons et al., 2007) indicate that the
203 typical order of crystallisation beneath Floreana is olivine, followed by clinopyroxene, with little to no
204 crystallisation of plagioclase.

205 # 4 ANALYTICAL METHODOLOGY

206 ## 4.1 Electron microprobe analysis

207 Glass chips, olivine and clinopyroxene crystals were hand-picked from crushed scoria and lava
208 samples, mounted in epoxy or indium, and then ground and polished prior to analysis (crystals
209 mounted in indium were polished individually prior to mounting). Xenolithic crystals were analysed
210 as individual crystals mounted in indium or *in situ* in petrographic thin sections. The major and minor
211 element concentrations of olivine, clinopyroxene and glass were measured using a Cameca SX100

electron microprobe in the Department of Earth Sciences, University of Cambridge. Calibrations were made using mineral and metal standards prior to each analytical session (see Gleeson and Gibson, 2019 for details). Glasses were analysed using a 6 nA, 15 kV, defocused (5 μm) beam for most elements. Na and K were analysed first (10 s peak count time) to avoid alkali migration. Other elements were analysed with peak count times of 10 s (Si), 20 s (Fe), 30 s (Al, P, Ca, Mg), 40 s (Mn), or 60 s (Ti). Sulphur was analysed last using a 20 nA beam current and a 60 s peak count time.

Pyroxene compositions were determined by spot analyses using a 20 nA, 15 kV, focused (~1 μm) beam, with Na, K and Si analysed first (10 s). Element maps of Cr, Ti, and Al in key clinopyroxene crystals from the Floreana xenoliths were created using a 60 nA, 15 kV, focused (~1 μm) beam, with a dwell time of 150 ms. Cr counts were collected on a PET and a LIF crystal, Al counts were collected on two TAP crystals, and Ti counts were collected on a PET crystal. Olivine electron microprobe analysis was carried out using the method outlined in Gleeson and Gibson (2019).

Analytical uncertainties were tracked through analysis of appropriate Smithsonian Microbeam Standards (Jarosewich et al., 1980). Accuracy was typically between 98 and 102% for all phases. 2σ analytical precision of clinopyroxene and olivine analyses are typically better than 2–3% for major elements (>1 wt%) and typically ~5-10% for minor elements (<1 wt%). Similarly, the 2σ precision for glass analysis was typically <3% for major elements, ~5% for Na, and ~10% for K (see Supplementary Information).

## 4.2 Laser ablation Inductively Coupled Plasma Mass Spectrometry

Trace element concentrations were measured in the apparent cores (i.e. as exposed in the 2D plane) of clinopyroxene crystals from scoria and xenolith samples using an ESI193 laser coupled to a Nexion 350D inductively coupled plasma mass spectrometer in the Department of Earth Sciences, University of Cambridge. Analyses were collected in spot mode using a 20 Hz laser repetition rate, 4 J/cm$^2$ fluence and 80 μm spot size, or in transect mode using a 10 Hz repetition rate, 3.5 J/cm$^2$ fluence and 30 μm spot size. For transects, individual spots were offset into two (alternating) lines to increase the spatial resolution. Laser ablation inductively coupled plasma mass spectrometry (LA-ICP-MS) data

reduction was carried out in Iolite©, with NIST 612SRM as the standard reference material (Hinton, 1999) and $^{43}Ca$ (from electron microprobe analysis) as the internal reference standard. Analytical accuracy was tracked using a USGS glass standard (Jochum et al., 2016) and was between 95% and 105% for most elements (See Supplementary File). 2σ analytical precision of spot analyses were monitored through analysis of an in-house clinopyroxene standard and was 5–10% for the light rare-earth elements (LREE), Y, Sr, and Zr and 10–20% for the heavy rare earth element (HREE). 2σ analytical precision was ~10% for all elements of interest in transect analyses (Ce, Y).

# 5 GLASS AND MINERAL CHEMISTRY

## 5.1 Matrix glass compositions

The matrix glass compositions measured in one scoria (17MMSG16) and two glassy lava samples (17MMSG12 and 17MMSG27) from Floreana have very similar MgO concentrations (mean concentrations of 6.06–6.67 wt%) but exhibit differences in the concentrations of other elements (Fig. 4). For example, sample 17MMSG12 has consistently lower $TiO_2$ and $Al_2O_3$ concentrations than 17MMSG16, which must either reflect heterogeneity in the composition of primary mantle melts or variations in crustal processing (e.g. the extent of plagioclase or clinopyroxene crystallisation; Fig. 4A,D). The largest variation in the glass major element composition, however, is seen in sample 17MMSG27 where, at a near constant MgO contents, the CaO, $Na_2O$, and $K_2O$ contents vary by ~6 wt%, 4.5 wt%, and 1.5 wt%, respectively (Fig. 4B,C). Differences between our matrix glass major element analyses and previously-published whole-rock data from Floreana (Harpp et al., 2014a) are primarily due to olivine accumulation in the whole-rock samples (additional accumulation of clinopyroxene may explain the high CaO content of some whole-rock samples; Fig. 4C).

Our Floreana matrix glass analyses have higher $Al_2O_3$ concentrations, at a given MgO content, than basaltic glass and whole-rock measurements from the western Galápagos Archipelago (excluding whole-rock samples with accumulated plagioclase, Fig. 4D; Geist et al., 2002). This indicates substantially lower extents of plagioclase fractionation in the Floreana magmatic system and is consistent with the scarcity of plagioclase phenocrysts in erupted Floreana lavas. Reduced plagioclase

crystallisation could be due to the major element composition or $H_2O$ content of primary mantle melts and/or increased pressure of magma storage (Asimow and Langmuir, 2003; Neave et al., 2019; Thompson, 1987; Winpenny and Maclennan, 2011).

## 5.2 Olivine compositions

Olivine crystals in our Floreana lava and scoria samples show large variations in their forsterite contents (Fo = 70–92, where Fo=(Mg/(Mg+$Fe^{2+}$) molar) with histograms showing a primary density peak at Fo~85 (Fig. 5), more primitive than the olivine compositions in equilibrium with basaltic glasses from Floreana ($K_D$=0.27-0.34, assuming a $Fe^{3+}/Fe_{tot}$ ratio of 0.15; Matzen et al., 2011; Peterson et al., 2015; Roeder and Emslie, 1970). Although there is no clear correlation between Fo and Ca concentration in these crystals, the most forsteritic olivines (Fo>83) have extremely diverse Ca contents (~250 to ~2600 ppm; Fig. 5), whereas crystals with lower Fo contents (<83) have ubiquitously low Ca concentrations (<1500 ppm). All crystals with >1500 ppm Ca are classified as Group 1 olivines. Crystals with <1500 ppm Ca, however, may be classified in any of the 5 olivine groups, with the most evolved crystals (Fo ~70) the only to display the sieve-like rim texture of Group 4 olivines.

Floreana olivines separated from the lava and scoria samples also have a large range of Ni concentrations (~700 to ~3200 ppm), consistent with crystallisation from a peridotite-derived melt (Fig. 5; Gleeson and Gibson, 2019; Herzberg, 2011; Matzen et al., 2017b, 2017a). All olivine crystals analysed in the wehrlite and dunite xenoliths have a narrow range of Fo contents (83-87) and, crucially, have uniformly low Ca concentrations (<1000 ppm) and moderately high Ni contents (~2000 ppm). Core-rim profiles were performed on a small number of the wehrlitic olivines, revealing typically flat profiles in Fo, Ni, and Ca, with one profile displaying evidence for an increase in Ca in the outer 10 – 20 μm (see Supplementary Information). The range in Ca contents of the Floreana olivines contrasts with isolated olivine crystals from other Galápagos islands where Ca is typically >1000 ppm (Gleeson and Gibson, 2019; Vidito et al., 2013). The Ca and Ni contents of our Floreana olivines are inversely related at a set Fo content (Fig. 5B).

## 5.3 Clinopyroxene compositions

### *5.3.1 Major elements*

The Floreana clinopyroxenes separated from the scoria and xenolith samples are augitic, and have a relatively high Mg# (0.85–0.90; Mg# = Mg/(Mg+$Fe_t$) molar). The clinopyroxenes reach high Na concentrations up to 1.58 wt% $Na_2O$ (0.11 Na atoms per formula unit; Fig. 6A) and, correspondingly, up to 10% of the jadeite component. In general, clinopyroxene separates from scoria samples display a wide range of Na concentrations, although some xenolithic clinopyroxenes extend to higher Na contents (Fig. 6A). The Floreana clinopyroxenes display a large range of Cr contents, ranging from <0.05 wt% in the most evolved crystals to ~1.72 wt% in the more primitive crystals (Fig. 6B). Clinopyroxene analyses are typically taken from the cores of crystals, but zoning was characterised by a series of transects (and maps) on the xenolithic clinopyroxenes (see Supplementary Information). Results indicate that the clinopyroxenes are unzoned with respect to most element (including MgO and FeO), but some zoning is present in their $Al_2O_3$, $TiO_2$ and $Cr_2O_3$ contents. Specifically, clinopyroxene crystal rims are typically characterised by elevated $TiO_2$, but lower $Cr_2O_3$ contents.

### *5.3.2 Trace elements*

Our Floreana clinopyroxenes display a wide range of geochemical enrichment, with LREE to MREE ratios varying from $[La/Sm]_n$ ~0.2 to $[La/Sm]_n$ ~3.1 (where n represents normalisation to the primitive mantle composition of Sun and McDonough, 1989). Wehrlitic clinopyroxenes typically have more enriched trace element ratios (such as $[La/Sm]_n$ or $[Ce/Y]_n$) than clinopyroxenes from the scoria samples (Fig. 7). Furthermore, melt $[La/Sm]_n$ ratios calculated to be in equilibrium with clinopyroxenes from the scoria and xenolith samples range from ~1 to ~15 (calculated using the major element composition of the clinopyroxene at the location of LA-ICP-MS analysis and the elastic strain model of Wood and Blundy (1997) at 1225°C and 700 MPa; Fig. 7B), significantly greater than the range measured in Floreana whole-rock samples (~2–5, with a small number of outliers up to ~7.5; Harpp et al. 2014a). Almost all of the xenolithic crystals, and a large proportion of the clinopyroxenes separated from scoria deposits, are too enriched to be in equilibrium with the typical composition of melts erupted on Floreana (Harpp et al.,2014a). In addition, there is a strong

correlation between the Na concentrations and highly/moderately incompatible trace element ratios of the Floreana clinopyroxenes ($p<10^{-3}$), such that crystals with enriched trace element signatures typically contain a high jadeite component (Fig. 7A). Finally, the Floreana clinopyroxenes all contain Eu anomalies ($Eu^* = Eu_n/\sqrt{Sm_n \times Gd_n}$) within analytical uncertainty of 1, and Sr anomalies ($Sr^* = Sr_n/\sqrt{Pr_n \times Nd_n}$) that have a similar range to that observed in the erupted basalts (Harpp et al., 2014a).

# 6 MAGMA SYSTEM ARCHITECTURE BENEATH ISLA FLOREANA

## 6.1 Mush crystallisation and textural equilibration

Based on pyroxene trace element and radiogenic isotope ratios, Lyons et al. (2007) hypothesised that gabbroic xenoliths in the Floreana lava and scoria deposits formed in an ancient (>1-1.5 Ma) magmatic system, compositionally similar to those currently beneath Cerro Azul and Sierra Negra volcanoes in the western Galápagos. In contrast, wehrlite xenoliths preserve isotopic ratios similar to more recent subaerial lavas on Floreana, suggesting that they are fragments of the present-day magmatic system (Lyons et al., 2007).

Our wehrlitic xenoliths preserve an original poikilitic igneous texture (clinopyroxene oikocrysts surrounding olivine chadacrysts) and display no evidence for the metamorphic breakdown of plagioclase (e.g. pseudomorphs or relict cores) as hypothesised by Lyons et al. (2007). We suggest that the clinopyroxene crystals in our wehrlitic xenoliths grew within an olivine-dominated cumulate mush (i.e. interstitial growth of clinopyroxene oikocrysts; Wager et al., 1960). If clinopyroxene growth is principally within a crystal-rich (i.e. relatively viscous and immobile) mush zone, this could explain its relatively low abundance in Floreana lava and scoria deposits (<5% of separated crystals).

In contrast, plagioclase triple junctions in the gabbroic xenoliths have ~120° dihedral angles (Fig. 3A), indicating a high degree of textural equilibration (Holness et al., 2019, 2005). Plagioclase textural equilibrium, along with the two-pyroxene phase assemblage, suggests that the gabbroic xenoliths

represent magmatic cumulates which were stored at high temperatures (>900ºC) on long timescales (Holness et al., 2006). These petrographic observations are consistent with the gabbroic nodules sampling an ancient magmatic system beneath Floreana (>1 Ma; Lyons et al., 2007).

## 6.2 Mush disaggregation prior to eruption

### *6.2.1 Insights from olivine compositional heterogeneity*

Olivine crystals separated from the Floreana lava and scoria samples have a wide range of zoning patterns, morphologies, and compositions (Fig. 2). The five olivine groups identified in the Floreana samples have distinct morphologies and zoning patterns (see Section 2 above), suggesting chemically heterogeneous magma storage (Holness et al., 2019). In particular, the most evolved crystals (Group 4; Fo~70–75) are in equilibrium with melts that are more evolved than the Floreana erupted basalts (likely basaltic andesites). This is consistent with a recent study which identified highly evolved (andesitic - dacitic) magmas beneath basaltic volcanoes in the western Galápagos Archipelago (Stock et al., 2020).

As Fe-Mg interdiffusion in olivine is geologically fast (Chakraborty, 2010; Costa et al., 2020), preservation of forsterite zoning in the Floreana olivine crystals suggests that multiple magma batches interacted on relatively short pre-eruptive timescales. In Group 5 olivines, for example, four compositional zones are preserved over ~100-200 μm (Fig. 2E and F). Whilst we do not have enough Group 5 olivine crystals to calculate statistically robust timescales of pre-eruptive magma interactions using diffusion chronometry, complex forsterite zoning over ~100 μm is estimated to last <3 yrs at the approximate temperature of basaltic magma storage (~1225ºC; using diffusion coefficients from Chakraborty, 2010). Therefore, we suggest that the range of crystal morphologies and major element compositions displayed by the Floreana olivines in lava and scoria deposits indicates mixing of chemically heterogeneous magma storage regions over relatively short timescales prior to eruption.

The minor element chemistry of the olivine crystals allows us to investigate the crystallinity of these chemically diverse magma storage regions. Olivine crystals in our Floreana lava and scoria deposits have an unusually low, and large range of Ca concentrations (~250–2600 ppm compared with ~1500-3000 ppm in the eastern Galápagos; Gleeson and Gibson, 2019; Fig. 5A). The lower end of the range

in Ca concentrations measured in the Floreana lava and scoria deposits overlaps with those observed in cumulate xenoliths (wehrlites) and thus are unlikely to represent mantle olivines (Thompson and Gibson, 2000). Previous studies have shown that the Ca concentration of magmatic olivine is sensitive to several parameters, including: (i) the major element composition of the co-existing melt phase (Herzberg, 2011); (ii) the $H_2O$ content of the co-existing melt phase (Gavrilenko et al., 2016); and (iii) the temperature of the system (Adams and Bishop, 1982; Köhler and Brey, 1990; Shejwalkar and Coogan, 2013).

Variations in the Ca content of primary mantle melts are commonly hypothesised to result from the presence of a lithologically heterogeneous mantle source (Herzberg, 2011; Sobolev et al., 2007; Vidito et al., 2013). Specifically, melting of a pyroxene-rich mantle lithology is expected to produce Ca-poor and Ni-rich melts which would go on to form Ca-poor, but Ni-rich, olivines. While the low Ca contents of many of the Floreana olivines would therefore appear to indicate derivation from melts of a pyroxenitic source lithology, the olivine Ni contents are relatively low (<3000 ppm), inconsistent with this hypothesis (Fig. 5B; Gleeson and Gibson, 2019). As a result, if the low Ca contents of the Floreana olivines represent equilibrium with low Ca melts, we require a different process to generate these compositions. This process must reduce the Ca concentration of the melt phase (and co-existing olivines), without simultaneously reducing the melt Mg# (as low Ca concentrations are observed across the entire range of forsterite contents in the Floreana olivines; Fig. 5A).

Evidence for the origin of the low-Ca contents in the Floreana olivines from lava and scoria deposits is present in the texture and composition of the wehrlitic xenoliths, which contain uniformly low-Ca olivine crystals (<1000 ppm; Fig. 5A). The petrography of the wehrlitic xenoliths attests to clinopyroxene growth within olivine-dominated mush regions. Clinopyroxene crystallisation within this mush would extract CaO and MgO from the residual melt. However, in an olivine-rich mush, the large reservoir of MgO contained within the cumulus olivine grains would buffer the residual melt at a near-constant Mg# during clinopyroxene crystallisation (Meyer et al., 1989). In contrast, the CaO concentration of the melt is not buffered and decreasing melt CaO contents, due to clinopyroxene crystallisation, will cause the CaO concentration of cumulus olivine grains to decrease (as a result of

diffusive re-equilibration). Support for this interpretation comes from the anomalously low CaO concentrations in the matrix glass of sample 17MMSG27.

Intercumulus clinopyroxene growth would also increase the $H_2O$ concentration of the residual melt phase, decreasing the partition coefficient of Ca into olivine (Gavrilenko et al., 2016). Therefore, variable amounts of clinopyroxene crystallisation within an olivine-dominated mush, and subsequent disaggregation of this mush by an ascending melt, could explain the range of Ca contents measured in the Floreana olivines derived from lava and scoria deposits. Specifically, we suggest that: (i) forsteritic olivine crystals (Fo>83) with Ca contents >1500 ppm are consistent with those expected from fractional crystallisation of mantle-derived melts in a liquid-rich magma storage region (Fig. 5A; Gleeson and Gibson, 2019); (ii) olivines with Ca contents <1000 ppm, overlapping with the wehrlitic olivines, reflect equilibrium with Ca-poor interstitial melts; and (iii) olivine crystals with intermediate Ca concentrations (1000 – 1500 ppm) are sourced from regions where clinopyroxene growth is less extensive, or ongoing at the time of eruption. Thus, the olivine crystal cargo of the Floreana magmas is predominantly derived from crystal-rich domains with only a small number of olivine crystals displaying compositions that are consistent with fractional crystallisation in liquid-rich storage regions (Ca >1500 ppm; Gleeson and Gibson, 2019).

It is an important to note, however, that the partitioning of Ca between co-existing olivine and clinopyroxene has been hypothesised to be sensitive to temperature (such that less Ca enters the olivine structure at lower temperature; Shejwalkar and Coogan, 2013). As a result, the heterogeneity in the Ca content of the Floreana olivines could instead represent disaggregation of xenolithic material that has undergone variable amounts of cooling. Both hypotheses presented here can recreate the range of Ca contents observed in the Floreana olivines and, as the majority of olivine analyses from the Floreana lava and scoria deposits have low Ca concentrations (<1000 ppm) that overlap with those in xenolithic nodules, indicate that a large proportion of the erupted crystal cargo derives from disaggregated, highly crystalline magma storage regions.

### *6.2.2 Insights from clinopyroxene major element compositions*

The compositions of clinopyroxene crystals from the Floreana scoria also overlap with those in our xenolith samples, supporting the hypothesis that some of the erupted crystals are derived from disaggregated sub-volcanic mush (Fig. 6). We used hierarchical cluster analysis to subdivide our 567 clinopyroxene major element analyses from the Floreana scoria and xenolith samples and determine the proportion of material that is derived from each xenolith lithology in the erupted crystal cargo (cluster analysis was performed in Python 3.8 using the scikit-learn package of Pedregosa et al. 2011). We find that our clinopyroxene analyses form three distinct clusters (Fig. 8):

- Cluster 1 clinopyroxenes are predominantly from the wehrlite and dunite xenoliths and include 90% of our analyses from these samples. 39% of clinopyroxenes analysed from the scoria samples also fall into this cluster.
- Cluster 2 clinopyroxenes include all analyses from the gabbroic xenoliths, and ~10% of analyses from crystals separated from the scoria samples.
- Cluster 3 clinopyroxenes are dominated by analyses of the scoria derived clinopyroxenes (~50% of analyses from the scoria separates). However, 10% of analyses from the wehrlite and dunite xenoliths also fall into this cluster.

Of our 248 clinopyroxenes analyses from the Floreana scoria, approximately half are classified as Cluster 3 and thus have major element compositions that do not show a clear chemical affinity to either the wehrlite/dunite or gabbroic cumulates. Therefore, these crystals may represent autocrysts (defined here as crystals that are genetically related to primary mantle melts beneath Floreana, but are not influenced by secondary cumulate processes) that grew in liquid-rich magma storage regions. The remainder of clinopyroxene analyses from the scoria are either compositionally analogous to those in the wehrlite and dunite xenoliths (Cluster 1; 39%) or the gabbroic xenoliths (Cluster 2; 11%); we interpret these as representing disaggregated sub-volcanic mush or wall rock. The high proportion of the clinopyroxene crystal cargo that is derived from highly crystalline storage regions beneath Floreana is consistent with our interpretation of olivine minor element concentrations.

## 6.3 Reactive Porous Flow within a cumulate mush

Whilst the olivine and clinopyroxene major and minor element concentrations show that a large proportion of the erupted crystal cargo is derived from highly crystalline magma storage regions, clinopyroxene trace element concentrations (and zoning) reveal the magmatic processes that operate within these crystal-rich domains. The trace element composition of melts in equilibrium with our clinopyroxene crystals are calculated using the model of Wood and Blundy (1997). The results indicate that many of our clinopyroxene analyses have incompatible trace element ratios (e.g. $[Ce/Y]_n$) which are more enriched than any erupted basalt from Floreana (Harpp et al., 2014a). In fact, nearly all clinopyroxene analyses from our xenolith samples, and ~50% of clinopyroxene analyses from the scoria samples, record trace element disequilibrium with the typical composition of the Floreana basalts (Fig. 7 and 9). Over-enriched trace element signatures are characteristic of Cluster 1 clinopyroxenes (i.e. chemical affinity to the wehrlitic or dunitic xenoliths), whereas crystals that are near trace element equilibrium with Floreana basalts typically have Cluster 3 major element compositions (i.e. the autocryst cluster).

Petrographic observations and olivine minor element data indicate that the Floreana sub-volcanic system is characterised by clinopyroxene crystallisation within an olivine-dominated mush. If the clinopyroxene grew from trapped melt within an olivine-dominated mush, progressive crystallisation would increase the concentration of highly incompatible trace elements (e.g. Ba, La, Ce) relative to less incompatible trace-elements (e.g. Sm, Y) in the residual melt. A simple fractional crystallisation model indicates that ~70% crystallisation is required to generate melt $[Ce/Y]_n$ ratios that are in equilibrium with enriched clinopyroxenes from the scoria samples and even greater extents of crystallisation (~80%) would be required to generate the extremely high $[Ce/Y]_n$ ratios in some of the xenolithic clinopyroxenes (Fig. 9).

Such extensive fractional crystallisation would be expected to result in the saturation and crystallisation of plagioclase and other accessory phases (e.g. apatite, magnetite/ilmenite, quartz), which are observed in more evolved xenoliths from Rabida island in the central Galápagos (Holness et al., 2019). However, these phases are absent in the Floreana xenoliths, indicating that either

474 infiltration of melts from a highly enriched mantle source component or a different magmatic process
475 within the cumulate mush is responsible for generating the anomalous trace element signatures of the
476 Floreana clinopyroxenes. Infiltration of mantle-derived melts that are more enriched than anything
477 observed in erupted basalts on Floreana is considered unlikely owing to the overlapping isotopic
478 composition of xenoliths and erupted lavas (Lyons et al., 2007), and the absence of a significant
479 correlation between trace element enrichment and radiogenic isotope compositions in the erupted
480 Floreana basalts (see Supplementary Information; Harpp et al., 2014a). As a result, a process other
481 than source heterogeneity must be responsible for generating the trace element variation in both the
482 Floreana xenoliths and erupted basalts.

483 One alternative mechanism that might be able to generate the observed trace element over-enrichment
484 is reactive porous flow. In this scenario, clinopyroxene is precipitated from ascending clinopyroxene-
485 saturated melts that continuously react with the existing, olivine-dominated crystal framework as the
486 system approaches equilibrium, and thus deviates from a simple fractional crystallisation trajectory
487 (Lissenberg and MacLeod, 2016). As a result, reactive porous flow in the olivine-dominated mush
488 beneath Floreana will likely result in substantial crystallisation of clinopyroxene, possibly at the
489 expense of pre-existing crystal phases, with little to no formation of olivine or saturation of minor
490 phases. Consequently, reactive porous flow can lead to enrichment of highly- to moderately-
491 incompatible trace elements in the resulting melt (Coogan et al., 2000; Gao et al., 2007; Lissenberg et
492 al., 2013; Lissenberg and MacLeod, 2016), and is consistent with the petrography of the Floreana
493 xenoliths. For example, major element maps of clinopyroxene crystals in the Floreana wehrlites show
494 that they are zoned, with Ti-rich rims (Fig. 10); equivalent zoning patterns have been attributed to
495 reactive porous flow in plutonic clinopyroxenes from the oceanic crust (e.g. Hess Deep; Lissenberg
496 and MacLeod, 2016). In addition, if pre-existing Cr-spinel was dissolved by the reacting melt, then
497 reactive porous flow could also explain the high Cr contents of clinopyroxene in our wehrlitic
498 xenoliths (Fig. 6; Lissenberg and MacLeod, 2016).

To test whether reactive porous flow of clinopyroxene saturated melts through an olivine-dominated mush is consistent with the trace element compositions of melts calculated to be in equilibrium with our Floreana clinopyroxenes, we use the zone refining model of Harris (1957; Fig. 9):

$$\frac{C_l}{C_l^o} = \frac{1}{D} - (\frac{1}{D} - 1)e^{-DI} \quad \text{(eq. 1)}$$

where $D$ is the bulk partition coefficient; $C_l^o$ and $C_l$ are the initial and final concentration of that element in the melt phase, respectively; and $I$ is the 'equivalent volumes of solid processed by the liquid' (Lissenberg and MacLeod, 2016). The model assumes continuous reaction of the percolating melt front with the existing crystal framework, and has previously been employed to investigate geochemical signatures in oceanic gabbros (Lissenberg and MacLeod, 2016). Results indicate that reactive porous flow can produce melts with trace element compositions that are comparable with those in equilibrium with our Floreana clinopyroxenes (i.e. $[Ce/Y]_n$ ~8-13) using $I$ values that are similar to those invoked in other magmatic settings worldwide (~2-5 compared to ~4-8 for the Hess Deep; Lissenberg and MacLeod, 2016). Hence, reactive porous flow represents a realistic mechanism for generating the geochemical diversity of Floreana clinopyroxenes, including the trace element enriched crystals analysed in the wehrlitic nodules (Fig. 9).

In addition, detailed LA-ICP-MS transects of two clinopyroxene grains from the most enriched wehrlitic xenolith analysed in this study (17MMSG02c) show clear trace element zoning (Fig. 11). The core of the larger clinopyroxene crystal has low [Ce] and $[Ce/Y]_n$ contents that are approximately in equilibrium with Floreana basalts (Harpp et al. 2014a; Fig. 11a), whereas the mantle and rim of the crystal is characterised by increasing [Ce] and $[Ce/Y]_n$ contents. We interpret this as core crystallisation from a melt with a trace element signature similar to that of erupted Floreana basalts (Harpp et al., 2014a), followed by growth from a melt which became progressively enriched during reactive porous flow (Fig. 11).

The mantle of the second, smaller xenolithic clinopyroxene shows a similar rim-ward increase in [Ce] (interpreted as progressive melt enrichment during reactive porous flow). However, the [Ce] and $[Ce/Y]_n$ values of the crystal core are too high to be in equilibrium with erupted Floreana basalts (Fig. 11C). This is consistent with our spot analyses of clinopyroxene cores in other crystals and samples. The high [Ce] and $[Ce/Y]_n$ values measured in crystal cores cannot be explained by inward diffusion of Ce, owing to significant differences in the diffusivities of Ce and Y and similar [Ce] and [Y] zoning patterns in our two crystal transects (Fig. 11; Van Orman, 2001). Instead, we suggest that the high apparent core [Ce] and $[Ce/Y]_n$ contents in many of the Floreana clinopyroxenes record crystallisation from melts that had already undergone geochemical enrichment via reactive porous flow. However, we cannot discount that our apparent clinopyroxene cores are fragments of larger oikocrysts that have been broken during mush disaggregation or sample crushing and, as a result, do not represent the true core compositions of each crystal.

Nevertheless, our clinopyroxene major and trace element data, as well as petrographic observations of the wehrlitic xenoliths, provide substantial evidence that reactive porous flow is an important mechanism of melt migration and melt differentiation in highly crystalline magma storage regions beneath Floreana. Although reactive porous flow has been identified as an important process in MOR gabbros, this is the first study to identify reactive porous flow in an ocean island setting.

## 6.4 Petrographic estimates of magma storage pressures

Petrological and geophysical constraints on magma storage depths exist for several recently active volcanoes in the western Galápagos Archipelago (Bagnardi et al., 2013; Case et al., 1973; Geist et al., 1998; Stock et al., 2018; Vigouroux et al., 2008). However, in the absence of geophysical data (owing to a paucity of recent eruptions), there are far fewer constraints on the structure of magma storage regions in the eastern and south-eastern archipelago. To date, the only investigation of magma storage depths beneath these volcanoes is by Geist et al. (1998), who undertook a visual comparison between whole-rock lava compositions and the MORB olivine + plagioclase + augite + melt pseudoinvariant point, parameterised by Grove et al. (1992). This approach is subject to substantial uncertainty, but the

549 authors suggest that the Floreana magmas consistently equilibrate at >5 kbar (typically >7 kbar) at a
550 depth >16 km, within the upper mantle.

551 We used three petrological barometers to provide improved constraints on magma storage depths
552 beneath Floreana. First, we applied the clinopyroxene-only barometer and thermometer of Putirka
553 (2008; equations 32b and 32d, respectively), in which pressure and temperature are solved iteratively
554 based solely on the clinopyroxene major element composition (primarily the jadeite component;
555 standard error of estimate [SEE] ±310 MPa). Second, we applied the clinopyroxene-melt barometer of
556 Neave and Putirka (2017; equation 1), which uses the composition of a co-existing melt phase and the
557 proportion of the Jadeite component in clinopyroxene to calculate the pressure of crystallisation (SEE
558 = ±140 MPa; pressure is solved iteratively with temperature using the clinopyroxene-melt
559 thermometer of Putirka, 2008; equation 33). Third, for the xenolithic nodules, we estimate the final
560 pressure and temperature of storage using the two-pyroxene thermobarometer of Putirka (2008;
561 equations 36 and 39; SEE = ±280 MPa).

562 Taken at face value, initial application of the clinopyroxene-only barometer to all clinopyroxene
563 analyses from the scoria and xenolith samples gives a range of pressure estimates between ~450 MPa
564 and ~1800 MPa. However, reactive porous flow has a substantial influence on the compositions of the
565 Cluster 1 (and Cluster 2) clinopyroxenes, which may influence the barometric results. Specifically,
566 crystals that show evidence for reactive porous flow also have elevated Na concentrations, leading to
567 an anomalously high jadeite component and thus calculated pressure. This likely originates from the
568 presence of unusual melt compositions that fall outside the calibration range of the clinopyroxene-
569 only barometer owing to reactive melt migration, which is supported by the unusual glass
570 compositions in sample 17MMSG27 (Fig. 4). Therefore, we filter our dataset to remove crystals that
571 show a chemical signature indicative of reactive porous flow and only use Cluster 3 clinopyroxenes
572 that have trace element compositions in equilibrium with the Floreana basalts (using the whole-rock
573 data from Harpp et al. 2014) in our barometric calculations (n=78). Barometric results from this
574 filtered dataset indicate that crystallisation beneath Floreana occurs at a pressure of 766 ±322 MPa

(2σ of calculated pressures), which equates to a depth of 25.2 ±9.9 km (using the crustal density estimate of Putirka (1997) and a mantle density estimate of 3300 kg/m$^3$; Fig. 12).

Application of the Neave and Putirka (2017) clinopyroxene-melt barometer requires identification of equilibrium clinopyroxene-liquid pairs. We achieve this using an automated melt-matching algorithm (as in Winpenny and Maclennan, 2011, Neave and Putirka, 2017, Stock et al. 2018), with $K_D$(Fe-Mg), diopside-hedenbergite, enstatite-ferrosillite and calcium Tschermak's equilibrium tests ($K_D$(Fe-Mg) within ±0.03 other components within 2 SEE; Putirka, 1999, Putirka, 2008, Mollo et al., 2013). We used the whole-rock data of Harpp et al. (2014a) and basaltic glass analyses from this study as potential equilibrium liquids. Input crystal compositions were again filtered to remove analyses that showed evidence of reactive porous flow (i.e. only Cluster 3 clinopyroxenes in trace element equilibrium with the Floreana whole-rock were used). In total, 70 of the 78 input clinopyroxene analyses returned at least one equilibrium match to either the basaltic glass or whole-rock compositions. Where clinopyroxene compositions produced an equilibrium match with more than one melt composition, an average melt composition was used in the barometric model. Results from this barometer, coupled to the thermometer of Putirka (2008), indicate that magma crystallisation occurred at 717 ±165 MPa (23.7 ±5.1 km) and 1224 ±33ºC (Fig. 12).

Clinopyroxene-orthopyroxene thermobarometry records the final storage conditions of the cumulate xenoliths, rather than the crystallisation conditions of clinopyroxene autocrysts (orthopyroxene is only found as an intercumulus phase). Temperature and pressure estimates were only calculated from orthopyroxene-clinopyroxene pairs in wehrlite and dunite xenoliths that passed the $K_D$(Fe-Mg) equilibrium test of Putirka (2008; 1.09 ±0.14). Results suggest that the cumulates were stored at ~975–1100ºC and 600–900 MPa, with a mean storage pressure of 712 ±200 MPa (23.7 ±6.4 km; Fig. 12).

The depths of magma storage calculated from our three petrological barometers show an excellent agreement within the model uncertainties. These new data provide robust evidence that magma storage beneath Floreana occurs below the Moho (~16 km; Feighner and Richards, 1994), in the upper mantle.

# 7 IMPLICATIONS FOR MAGMATIC PLUMBING SYSTEMS BENEATH LOW MELT FLUX OCEAN ISLAND VOLCANOES

Our new petrological and geochemical data show that magma storage beneath Floreana occurs in mush-dominated regions of the upper mantle (Fig. 13). Mineral chemistry (such as low olivine Ca concentrations and clinopyroxene major elements) reveal that a substantial portion of the erupted crystal cargo is derived from disaggregated mush and wall rock material which has been entrained into the ascending magmas. During ascent, magmas may entrain coherent nodules (xenoliths) as well as disaggregated mush (Fig. 13). Coherent nodules represent areas of the magmatic system beneath Floreana that have undergone cooling to temperatures <1100ºC (compared to the clinopyroxene crystallisation temperatures of ~1225ºC) and may represent material from the border of the active mush zone or older, almost completely solidified magma storage regions that are intersected during magma ascent (Fig. 13).

Petrographic observations and clinopyroxene trace element chemistry from both the xenolith and scoria samples reveal that clinopyroxene growth occurs via reactive porous flow in the mush-dominated areas beneath Floreana. Reactive porous flow causes distinct trace element enrichment in the percolating melt phase and crystallising clinopyroxene, which can explain the trace element disequilibrium between the erupted Floreana basalts and their clinopyroxene cargo. Nevertheless, the presence of some clinopyroxene crystals with major and trace element compositions in equilibrium with erupted Floreana basalts indicates that at least some crystallisation occurs in liquid-rich sub-volcanic storage regions, likely situated as localised melt pockets within the larger mush zone (Fig. 13).

Transport of melts modified by reactive porous flow into these melt pockets could impact the LREE enriched signature of the resultant hybridised melts. This could help to explain the unique, concave up REE signature of the Floreana basalts, which is not seen in other regions of the Galápagos Archipelago (Harpp et al., 2014a). However, it is important to note that similar trace element signatures are not observed in other, low melt-flux regions of the eastern Galapagos (such as San

629 Cristobal; Geist et al., 1986). As a result, we hypothesise that the unique REE pattern of the Floreana
630 basalts is primarily a source signature, likely associated with the highly radiogenic Pb and Sr isotope
631 signatures that characterise the Floreana basalts (Harpp et al., 2014a; Harpp and White, 2001).
632 Nevertheless, a few basalts on Floreana have trace element signatures that are far more enriched than
633 the majority of erupted basalts ($[La/Sm]_n$ up to 7.5), but are isotopically indistinguishable (Harpp et
634 al., 2014a); we therefore suggest that these basalts contain an anomalously large contribution of melts
635 that have undergone geochemical modification due to reactive porous flow.

636 Our results indicate substantial differences in the architecture of the magmatic systems beneath
637 Floreana and the frequently active shield volcanoes in the western Galápagos Archipelago. For
638 example, previous petrological and geophysical studies have identified that western Galápagos
639 magmatic systems are characterised by crustal magma storage, often with a large storage region in the
640 mid-to-lower crust (~7 km depth) and a smaller storage region at shallow levels, within the volcanic
641 edifice (~1 km depth; Geist et al. 1998; Bagnardi et al. 2013; Bagnardi and Hooper, 2018; Stock et al.,
642 2018; Fig 12). In contrast, our barometric data indicate that magmas beneath Floreana ascend directly
643 from the upper mantle and undergo no detectable crustal storage. In addition, although mush-rich
644 regions have been inferred beneath the western Galápagos shield volcanoes (based on whole-rock data
645 and the presence of gabbroic glomerocrysts; Chadwick et al., 2011; Geist et al., 1995, 2014; Stock et
646 al., 2018), magmatic differentiation appears to be driven by simple fractional crystallisation and
647 mixing of chemically diverse magmas (Geist et al., 1995; Naumann and Geist, 1999; Stock et al.,
648 2020).

649 One major factor that differentiates Floreana from shield volcanoes in the western archipelago is the
650 flux of magma into the lithosphere, which is evidenced by the large variations in the volumetric
651 eruption rate on Floreana and the western shields (Harpp et al., 2014a; Harpp and Geist, 2018; Kurz et
652 al., 2014). Hence, we suggest that the greater pressure of magma storage and prevalence of reactive
653 porous flow beneath Floreana, relative to volcanoes in the western archipelago, are related to the
654 substantially lower flux of magma into the lithosphere from the underlying mantle source (and thus
655 the thermal structure of the lithosphere). For example, the magma flux entering the lithosphere

beneath Wolf volcano (northern Isabela) has been substantially greater than that beneath Floreana for several 100,000s of years (Geist et al., 2005). The high magma flux beneath Wolf maintains the average temperature of the mid-to-lower crust at ~1125ºC (ΔT ~22 ºC), with only small-scale thermal and compositional heterogeneities present in the sub-volcanic plumbing system (Geist et al., 2014, 2005; Stock et al., 2020, 2018). In contrast, the flux of magma entering the magmatic system beneath Floreana is much lower and the temperature of the mid-crust is likely to be significantly cooler than the lowest temperature recorded by the Floreana xenoliths (that is, <<900ºC; Fig. 12). As the flux of magma (and heat) from the mantle is insufficient to maintain an elevated crustal geotherm beneath Floreana, magmas that stall in the crust are likely to rapidly crystallise, increase their viscosity, and become uneruptable. Therefore, eruptions must be fed by melts ascending from much deeper storage regions (~700-750 MPa) where melts can persist over long time periods.

Our results have global implications for the architecture and dynamics of magma storage regions beneath ocean island volcanoes worldwide. The observed difference in magma storage depths beneath high and low melt flux volcanic systems in the Galapagos Archipelago is mirrored in a global compilation of barometric data from ocean island volcanoes (Famin et al., 2009; Geist et al., 1998; Hammer et al., 2016; Hartley et al., 2018; Klügel et al., 2015; Poland et al., 2015; Stock et al., 2018; Zanon et al., 2020; Zanon and Pimentel, 2015). Using the average repose period between eruptions at a particular basaltic volcanic centre as a proxy for the flux of magma entering the lithosphere from the underlying mantle (Global Volcanism Program, 2013), Figure 14 shows that the most frequently active volcanic centres (such as, Kīlauea, Hawai'i, and Piton de la Fournaise, Réunion) are characterised by persistent magma storage in the mid to upper crust (Famin et al., 2009; Poland et al., 2015). In contrast, less active centres located above low buoyancy flux plumes (e.g. El Hierro, Canary Islands) and/or peripheral to the main zone of plume upwelling (e.g. Haleakalā, Hawai'i) are characterised by longer repose periods and correspondingly greater magma storage pressures (Hammer et al., 2016; Klügel et al., 2015; Zanon and Pimentel, 2015). In fact, although secondary crustal magma staging can occur (Klügel et al., 2015), the main zone of magma storage beneath ocean island volcanoes with repose periods >50 years is typically in the lithospheric mantle, below the base

of the crust (Longpre et al., 2014; Taracsák et al., 2019; Zanon et al., 2020). Hence, we speculate that the flux of magma from the underlying mantle source has a first-order control on the depth of magma storage beneath ocean island volcanoes and, correspondingly, high-pressure magma storage – as observed beneath Floreana – is characteristic of low melt flux ocean island volcanoes globally.

# 8 CONCLUSIONS

Petrographic and geochemical analyses of lava, scoria and xenolith samples from Floreana in the south-eastern Galápagos Archipelago provide new insights into the architecture and dynamics of magma storage beneath low melt flux ocean island volcanoes. Comparison of olivine and clinopyroxene major, minor and trace element contents between our different sample types reveal that a substantial portion of the erupted crystal cargo is derived from mush-dominated magma storage regions beneath Floreana. Mineral textures, highly enriched clinopyroxene trace element signatures and trace element zoning in the xenoliths reveals that reactive porous flow is an important process of chemical differentiation and melt transport within these mush-dominated regions. Mixing between melts that have been geochemically enriched by reactive porous flow and those in overlying liquid-rich storage regions could contribute to the anomalous, concave-up REE signature of the Floreana basalts, which is absent in other parts of the Galápagos Archipelago where reactive porous flow has not been identified.

Application of independent petrological barometers to crystals in Floreana scoria and xenolith samples indicates that magmas are stored in the upper mantle (~23.7 ±5.1 km). Floreana is in a distal location to the Galápagos plume where the melt flux entering the lithosphere is low; the depth of magma storage beneath Floreana contrasts with more proximal, higher melt flux volcanoes in the western archipelago where magmas are stored in the crust (Geist et al., 1998; Stock et al., 2018). Comparing our new data with ocean island volcanoes globally (e.g. Hawai'i, Iceland and the Canary Islands) reveals that the Galápagos is not unique and that magma storage is ubiquitously shallower in proximal magmatic systems above high buoyancy flux plumes than in off-axis systems, or above low buoyancy flux plumes. We therefore suggest that the flux of mantle-derived magma entering the

lithosphere imparts a first-order control on the depth of magma storage beneath ocean island volcanoes.

## ACKNOWLEDGEMENTS

This study was supported by a NERC (Natural Environmental Research Council) Research Training Student Grant (NE/L002507/1) awarded to M.L.M.G as well as NERC grant awarded to S.A.G RG57434. M. J. S. was supported by a Charles Darwin and Galápagos Islands Junior Research Fellowship at Christ's College, Cambridge. We are grateful to Iris Buisman and Jason Day for their help with electron microprobe and laser-ablation inductively-coupled mass spectrometry analysis, respectively. We also thank Margaret Hartley and John Maclennan for their comments on an early version of this manuscript, as well as Dennis Geist and two anonymous reviewers for their helpful comments that greatly improved this manuscript.

## REFERENCES

Adams, G.E., Bishop, F.C., 1982. Experimental investigation of CaMg exchange between olivine, orthopyroxene, and clinopyroxene: potential for geobarometry. Earth Planet. Sci. Lett. 57, 241–250. https://doi.org/10.1016/0012-821X(82)90188-1

Allan, J.F., Simkin, T., 2000. Fernandina Volcano's evolved, well-mixed basalts: Mineralogical and petrological constraints on the nature of the Galapagos plume. J. Geophys. Res. Solid Earth 105, 6017–6041. https://doi.org/10.1029/1999JB900417

Amelung, F., Jónsson, S., Zebker, H., Segall, P., 2000. Widespread uplift and 'trapdoor' faulting on Galápagos volcanoes observed with radar interferometry. Nature 407, 993–996. https://doi.org/10.1038/35039604

Asimow, P.D., Langmuir, C.H., 2003. The importance of water to oceanic mantle melting regimes. Nature 421, 815–820. https://doi.org/10.1038/nature01429

Bagnardi, M., Amelung, F., Poland, M.P., 2013. A new model for the growth of basaltic shields based on deformation of Fernandina volcano, Galápagos Islands. Earth Planet. Sci. Lett. 377–378, 358–366. https://doi.org/10.1016/j.epsl.2013.07.016

Bailey, K., 1976. Potassium-Argon Ages from the Galapagos Islands. Science 192, 465–467. https://doi.org/10.1126/science.192.4238.465

Bernard, B., Stock, M.J., Coppola, D., Hidalgo, S., Bagnardi, M., Gibson, S., Hernandez, S., Ramón, P., Gleeson, M., 2019. Chronology and phenomenology of the 1982 and 2015 Wolf volcano eruptions, Galápagos Archipelago. J. Volcanol. Geotherm. Res. 374, 26–38. https://doi.org/10.1016/j.jvolgeores.2019.02.013

Bow, C.S., Geist, D.J., 1992. Geology and petrology of Floreana Island, Galapagos Archipelago, Ecuador. J. Volcanol. Geotherm. Res. 52, 83–105. https://doi.org/10.1016/0377-0273(92)90134-Y

Case, J.E., Ryland, S.L., Simkin, T., Howard, K.A., 1973. Gravitational Evidence for a Low-Density Mass beneath the Galapagos Islands. Science 181, 1040–1042. https://doi.org/10.1126/science.181.4104.1040

Chadwick, W.W., Howard, K.A., 1991. The pattern of circumferential and radial eruptive fissures on the volcanoes of Fernandina and Isabela islands, Galapagos. Bull. Volcanol. 53, 259–275. https://doi.org/10.1007/BF00414523

Chadwick, W.W., Jónsson, S., Geist, D.J., Poland, M., Johnson, D.J., Batt, S., Harpp, K.S., Ruiz, A., 2011. The May 2005 eruption of Fernandina volcano, Galápagos: The first circumferential

752 dike intrusion observed by GPS and InSAR. Bull. Volcanol. 73, 679–697.
753 https://doi.org/10.1007/s00445-010-0433-0
754 Chakraborty, S., 2010. Diffusion Coefficients in Olivine, Wadsleyite and Ringwoodite. Rev. Mineral.
755 Geochem. 72, 603–639. https://doi.org/10.2138/rmg.2010.72.13
756 Clague, D.A., Denlinger, R.P., 1994. Role of olivine cumulates in destabilizing the flanks of Hawaiian
757 volcanoes. Bull. Volcanol. 56, 425–434. https://doi.org/10.1007/BF00302824
758 Cleary, Z., Schwartz, D.M., Mittelstaedt, E., Harpp, K., 2020. Dynamic Magma Storage at Near-Ridge
759 Hot Spots: Evidence From New Galápagos Gravity Data. Geochem. Geophys. Geosystems 21.
760 https://doi.org/10.1029/2019GC008722
761 Coogan, L.A., Saunders, A.D., Kempton, P.D., Norry, M.J., 2000. Evidence from oceanic gabbros for
762 porous melt migration within a crystal mush beneath the Mid-Atlantic Ridge. Geochem.
763 Geophys. Geosystems 1, n/a-n/a. https://doi.org/10.1029/2000GC000072
764 Costa, F., Shea, T., Ubide, T., 2020. Diffusion chronometry and the timescales of magmatic processes.
765 Nat. Rev. Earth Environ. https://doi.org/10.1038/s43017-020-0038-x
766 Davidge, L., Ebinger, C., Ruiz, M., Tepp, G., Amelung, F., Geist, D., Coté, D., Anzieta, J., 2017.
767 Seismicity patterns during a period of inflation at Sierra Negra volcano, Galápagos Ocean
768 Island Chain. Earth Planet. Sci. Lett. 462, 169–179.
769 https://doi.org/10.1016/j.epsl.2016.12.021
770 Donaldson, C.H., 1976. An experimental investigation of olivine morphology. Contrib. Mineral.
771 Petrol. 57, 187–213. https://doi.org/10.1007/BF00405225
772 Famin, V., Welsch, B., Okumura, S., Bachèlery, P., Nakashima, S., 2009. Three differentiation stages
773 of a single magma at Piton de la Fournaise volcano (Reunion hot spot). Geochem. Geophys.
774 Geosystems 10, n/a-n/a. https://doi.org/10.1029/2008GC002015
775 Feighner, M.A., Richards, M.A., 1994. Lithospheric structure and compensation mechanisms of the
776 Galápagos Archipelago. J. Geophys. Res. 99, 6711. https://doi.org/10.1029/93JB03360
777 Gao, Y., Hoefs, J., Hellebrand, E., von der Handt, A., Snow, J.E., 2007. Trace element zoning in
778 pyroxenes from ODP Hole 735B gabbros: diffusive exchange or synkinematic crystal
779 fractionation? Contrib. Mineral. Petrol. 153, 429–442. https://doi.org/10.1007/s00410-006-
780 0158-4
781 Gavrilenko, M., Herzberg, C., Vidito, C., Carr, M.J., Tenner, T., Ozerov, A., 2016. A Calcium-in-Olivine
782 Geohygrometer and its Application to Subduction Zone Magmatism. J. Petrol. 57, 1811–
783 1832. https://doi.org/10.1093/petrology/egw062
784 Geist, D., Howard, K.A., Larson, P., 1995. The Generation of Oceanic Rhyolites by Crystal
785 Fractionation: the Basalt-Rhyolite Association at Volc n Alcedo, Gal pagos Archipelago. J.
786 Petrol. 36, 965–982. https://doi.org/10.1093/petrology/36.4.965
787 Geist, D., Naumann, T., Larson, P., 1998. Evolution of Galapagos Magmas: Mantle and Crustal
788 Fractionation without Assimilation. J. Petrol. 39, 953–971.
789 https://doi.org/10.1093/petroj/39.5.953
790 Geist, D., White, W.M., Albarede, F., Harpp, K., Reynolds, R., Blichert-Toft, J., Kurz, M.D., 2002.
791 Volcanic evolution in the Galápagos: The dissected shield of Volcan Ecuador. Geochem.
792 Geophys. Geosystems 3, 1 of 32–32 32. https://doi.org/10.1029/2002GC000355
793 Geist, D.J., Bergantz, G., Chadwick, W.W., 2014. Galápagos Magma Chambers, in: Harpp, K.S.,
794 Mittelstaedt, E., d'Ozouville, N., Graham, D.W. (Eds.), Geophysical Monograph Series. John
795 Wiley & Sons, Inc, Hoboken, New Jersey, pp. 55–69.
796 https://doi.org/10.1002/9781118852538.ch5
797 Geist, D.J., Fornari, D.J., Kurz, M.D., Harpp, K.S., Adam Soule, S., Perfit, M.R., Koleszar, A.M., 2006.
798 Submarine Fernandina: Magmatism at the leading edge of the Galápagos hot spot.
799 Geochem. Geophys. Geosystems 7, n/a-n/a. https://doi.org/10.1029/2006GC001290
800 Geist, D.J., McBIRNEY, A.R., Duncan, R.A., 1986. Geology and petrogenesis of lavas from San
801 Cristobal Island, Galapagos Archipelago. Geol. Soc. Am. Bull. 97, 555.
802 https://doi.org/10.1130/0016-7606(1986)97<555:GAPOLF>2.0.CO;2

Geist, D.J., Naumann, T.R., Standish, J.J., Kurz, M.D., Harpp, K.S., White, W.M., Fornari, D.J., 2005. Wolf Volcano, Galápagos Archipelago: Melting and Magmatic Evolution at the Margins of a Mantle Plume. J. Petrol. 46, 2197–2224. https://doi.org/10.1093/petrology/egi052

Geist, D.J., White, W.M., McBirney, A.R., 1988. Plume-asthenosphere mixing beneath the Galapagos archipelago. Nature 333, 657–660. https://doi.org/10.1038/333657a0

Gibson, S.A., Dale, C.W., Geist, D.J., Day, J.A., Brügmann, G., Harpp, K.S., 2016. The influence of melt flux and crustal processing on Re–Os isotope systematics of ocean island basalts: Constraints from Galápagos. Earth Planet. Sci. Lett. 449, 345–359. https://doi.org/10.1016/j.epsl.2016.05.021

Gibson, S.A., Geist, D., 2010. Geochemical and geophysical estimates of lithospheric thickness variation beneath Galápagos. Earth Planet. Sci. Lett. 300, 275–286. https://doi.org/10.1016/j.epsl.2010.10.002

Gibson, S.A., Geist, D.G., Day, J.A., Dale, C.W., 2012. Short wavelength heterogeneity in the Galápagos plume: Evidence from compositionally diverse basalts on Isla Santiago. Geochem. Geophys. Geosystems 13. https://doi.org/10.1029/2012GC004244

Gleeson, M.L.M., Gibson, S.A., 2019. Crustal controls on apparent mantle pyroxenite signals in ocean-island basalts. Geology. https://doi.org/10.1130/G45759.1

Gleeson, M.L.M., Gibson, S.A., Williams, H.M., 2020. Novel insights from Fe-isotopes into the lithological heterogeneity of Ocean Island Basalts and plume-influenced MORBs. Earth Planet. Sci. Lett. 535, 116114. https://doi.org/10.1016/j.epsl.2020.116114

Global Volcanism Program, 2013. Volcanoes of the World, v. 4.9.0 (04 Jun 2020). Venzke, E (ed.). Smithsonian Institution. Downloaded 24th Aug (2020).

Grove, T.L., Kinzler, R.J., Bryan, W.B., 1992. Fractionation of Mid-Ocean Ridge Basalt (MORB), in: Morgan, J.P., Blackman, D.K., Sinton, J.M. (Eds.), Geophysical Monograph Series. American Geophysical Union, Washington, D. C., pp. 281–310. https://doi.org/10.1029/GM071p0281

Hammer, J., Jacob, S., Welsch, B., Hellebrand, E., Sinton, J., 2016. Clinopyroxene in postshield Haleakala ankaramite: 1. Efficacy of thermobarometry. Contrib. Mineral. Petrol. 171, 7. https://doi.org/10.1007/s00410-015-1212-x

Harpp, K.S., Geist, D.J., 2018. The Evolution of Galápagos Volcanoes: An Alternative Perspective. Front. Earth Sci. 6. https://doi.org/10.3389/feart.2018.00050

Harpp, K.S., Geist, D.J., Koleszar, A.M., Christensen, B., Lyons, J., Sabga, M., Rollins, N., 2014a. The Geology and Geochemistry of Isla Floreana, Galápagos: A Different Type of Late-Stage Ocean Island Volcanism, in: Harpp, K.S., Mittelstaedt, E., d'Ozouville, N., Graham, D.W. (Eds.), Geophysical Monograph Series. John Wiley & Sons, Inc, Hoboken, New Jersey, pp. 71–117. https://doi.org/10.1002/9781118852538.ch6

Harpp, K.S., White, W.M., 2001. Tracing a mantle plume: Isotopic and trace element variations of Galápagos seamounts. Geochem. Geophys. Geosystems 2, n/a-n/a. https://doi.org/10.1029/2000GC000137

Harpp, K.S., Wirth, K.R., Teasdale, R., Blair, S., Reed, L., Barr, J., Pistiner, J., Korich, D., 2014b. Plume-Ridge Interaction in the Galápagos: Perspectives from Wolf, Darwin, and Genovesa Islands, in: Harpp, K.S., Mittelstaedt, E., d'Ozouville, N., Graham, D.W. (Eds.), Geophysical Monograph Series. John Wiley & Sons, Inc, Hoboken, New Jersey, pp. 285–334. https://doi.org/10.1002/9781118852538.ch15

Harris, P.G., 1957. Zone refining and the origin of potassic basalts. Geochim. Cosmochim. Acta 12, 195–208. https://doi.org/10.1016/0016-7037(57)90032-7

Hartley, M.E., Bali, E., Maclennan, J., Neave, D.A., Halldórsson, S.A., 2018. Melt inclusion constraints on petrogenesis of the 2014–2015 Holuhraun eruption, Iceland. Contrib. Mineral. Petrol. 173. https://doi.org/10.1007/s00410-017-1435-0

Herzberg, C., 2011. Identification of Source Lithology in the Hawaiian and Canary Islands: Implications for Origins. J. Petrol. 52, 113–146. https://doi.org/10.1093/petrology/egq075

Hinton, R.W., 1999. NIST SRM 610, 611 and SRM 612, 613 Multi-Element Glasses: Constraints from Element Abundance Ratios Measured by Microprobe Techniques. Geostand. Geoanalytical Res. 23, 197–207. https://doi.org/10.1111/j.1751-908X.1999.tb00574.x

Holness, M.B., Cheadle, M.J., McKENZIE, D., 2005. On the Use of Changes in Dihedral Angle to Decode Late-stage Textural Evolution in Cumulates. J. Petrol. 46, 1565–1583. https://doi.org/10.1093/petrology/egi026

Holness, M.B., Nielsen, T.F.D., Tegner, C., 2006. Textural Maturity of Cumulates: a Record of Chamber Filling, Liquidus Assemblage, Cooling Rate and Large-scale Convection in Mafic Layered Intrusions. J. Petrol. 48, 141–157. https://doi.org/10.1093/petrology/egl057

Holness, M.B., Stock, M.J., Geist, D., 2019. Magma chambers versus mush zones: constraining the architecture of sub-volcanic plumbing systems from microstructural analysis of crystalline enclaves. Philos. Trans. R. Soc. Math. Phys. Eng. Sci. 377, 20180006. https://doi.org/10.1098/rsta.2018.0006

Jackson, M.G., Konter, J.G., Becker, T.W., 2017. Primordial helium entrained by the hottest mantle plumes. Nature 542, 340–343. https://doi.org/10.1038/nature21023

Jarosewich, E., Nelen, J.A., Norberg, J.A., 1980. Reference Samples for Electron Microprobe Analysis*. Geostand. Geoanalytical Res. 4, 43–47. https://doi.org/10.1111/j.1751-908X.1980.tb00273.x

Jochum, K.P., Weis, U., Schwager, B., Stoll, B., Wilson, S.A., Haug, G.H., Andreae, M.O., Enzweiler, J., 2016. Reference Values Following ISO Guidelines for Frequently Requested Rock Reference Materials. Geostand. Geoanalytical Res. 40, 333–350. https://doi.org/10.1111/j.1751-908X.2015.00392.x

Kilbride, B.M., Edmonds, M., Biggs, J., 2016. Observing eruptions of gas-rich compressible magmas from space. Nat. Commun. 7, 13744. https://doi.org/10.1038/ncomms13744

Klügel, A., Longpré, M.-A., García-Cañada, L., Stix, J., 2015. Deep intrusions, lateral magma transport and related uplift at ocean island volcanoes. Earth Planet. Sci. Lett. 431, 140–149. https://doi.org/10.1016/j.epsl.2015.09.031

Köhler, T.P., Brey, G.P., 1990. Calcium exchange between olivine and clinopyroxene calibrated as a geothermobarometer for natural peridotites from 2 to 60 kb with applications. Geochim. Cosmochim. Acta 54, 2375–2388. https://doi.org/10.1016/0016-7037(90)90226-B

Kurz, M.D., Rowland, S.K., Curtice, J., Saal, A.E., Naumann, T., 2014. Eruption Rates for Fernandina Volcano: A New Chronology at the Galápagos Hotspot Center, in: Harpp, K.S., Mittelstaedt, E., d'Ozouville, N., Graham, D.W. (Eds.), Geophysical Monograph Series. John Wiley & Sons, Inc, Hoboken, New Jersey, pp. 41–54. https://doi.org/10.1002/9781118852538.ch4

Lissenberg, C.J., MacLeod, C.J., 2016. A Reactive Porous Flow Control on Mid-ocean Ridge Magmatic Evolution. J. Petrol. 57, 2195–2220. https://doi.org/10.1093/petrology/egw074

Lissenberg, C.J., MacLeod, C.J., Howard, K.A., Godard, M., 2013. Pervasive reactive melt migration through fast-spreading lower oceanic crust (Hess Deep, equatorial Pacific Ocean). Earth Planet. Sci. Lett. 361, 436–447. https://doi.org/10.1016/j.epsl.2012.11.012

Longpre, M.-A., Klugel, A., Diehl, A., Stix, J., 2014. Mixing in mantle magma reservoirs prior to and during the 2011-2012 eruption at El Hierro, Canary Islands. Geology 42, 315–318. https://doi.org/10.1130/G35165.1

Lyons, J., Geist, D., Harpp, K., Diefenbach, B., Olin, P., Vervoort, J., 2007. Crustal growth by magmatic overplating in the Galápagos. Geology 35, 511. https://doi.org/10.1130/G23044A.1

Mahr, J., Harpp, K S, Kurz, M D, Geist, D, Bercovici, H., Pimentel, R., Cleary, Z., 2016. Rejuvenescent Volcanism on San Cristóbal Island, Galápagos: A Late" Plumer". AGU Fall Abstr.

Matzen, A.K., Baker, M.B., Beckett, J.R., Stolper, E.M., 2011. Fe–Mg Partitioning between Olivine and High-magnesian Melts and the Nature of Hawaiian Parental Liquids. J. Petrol. 52, 1243–1263. https://doi.org/10.1093/petrology/egq089

902 Matzen, A.K., Baker, M.B., Beckett, J.R., Wood, B.J., Stolper, E.M., 2017a. The effect of liquid
903 composition on the partitioning of Ni between olivine and silicate melt. Contrib. Mineral.
904 Petrol. 172. https://doi.org/10.1007/s00410-016-1319-8
905 Matzen, A.K., Wood, B.J., Baker, M.B., Stolper, E.M., 2017b. The roles of pyroxenite and peridotite in
906 the mantle sources of oceanic basalts. Nat. Geosci. 10, 530–535.
907 https://doi.org/10.1038/ngeo2968
908 Meyer, P.S., Dick, H.J.B., Thompson, G., 1989. Cumulate gabbros from the Southwest Indian Ridge,
909 54�S-7� 16? E: implications for magmatic processes at a slow spreading ridge. Contrib.
910 Mineral. Petrol. 103, 44–63. https://doi.org/10.1007/BF00371364
911 Mollo, S., Putirka, K., Misiti, V., Soligo, M., Scarlato, P., 2013. A new test for equilibrium based on
912 clinopyroxene–melt pairs: Clues on the solidification temperatures of Etnean alkaline melts
913 at post-eruptive conditions. Chem. Geol. 352, 92–100.
914 https://doi.org/10.1016/j.chemgeo.2013.05.026
915 Naumann, T., Geist, D., 2000. Physical volcanology and structural development of Cerro Azul
916 Volcano, Isabela Island, Galápagos: implications for the development of Galápagos-type
917 shield volcanoes. Bull. Volcanol. 61, 497–514. https://doi.org/10.1007/s004450050001
918 Naumann, T.R., Geist, D.J., 1999. Generation of alkalic basalt by crystal fractionation of tholeiitic
919 magma. Geology 27, 423. https://doi.org/10.1130/0091-
920 7613(1999)027<0423:GOABBC>2.3.CO;2
921 Neal, C.A., Brantley, S.R., Antolik, L., Babb, J.L., Burgess, M., Calles, K., Cappos, M., Chang, J.C.,
922 Conway, S., Desmither, L., Dotray, P., Elias, T., Fukunaga, P., Fuke, S., Johanson, I.A.,
923 Kamibayashi, K., Kauahikaua, J., Lee, R.L., Pekalib, S., Miklius, A., Million, W., Moniz, C.J.,
924 Nadeau, P.A., Okubo, P., Parcheta, C., Patrick, M.R., Shiro, B., Swanson, D.A., Tollett, W.,
925 Trusdell, F., Younger, E.F., Zoeller, M.H., Montgomery-Brown, E.K., Anderson, K.R., Poland,
926 M.P., Ball, J.L., Bard, J., Coombs, M., Dietterich, H.R., Kern, C., Thelen, W.A., Cervelli, P.F.,
927 Orr, T., Houghton, B.F., Gansecki, C., Hazlett, R., Lundgren, P., Diefenbach, A.K., Lerner, A.H.,
928 Waite, G., Kelly, P., Clor, L., Werner, C., Mulliken, K., Fisher, G., Damby, D., 2019. The 2018
929 rift eruption and summit collapse of Kīlauea Volcano. Science 363, 367–374.
930 https://doi.org/10.1126/science.aav7046
931 Neave, D.A., Namur, O., Shorttle, O., Holtz, F., 2019. Magmatic evolution biases basaltic records of
932 mantle chemistry towards melts from recycled sources. Earth Planet. Sci. Lett. 520, 199–211.
933 https://doi.org/10.1016/j.epsl.2019.06.003
934 Neave, D.A., Putirka, K.D., 2017. A new clinopyroxene-liquid barometer, and implications for magma
935 storage pressures under Icelandic rift zones. Am. Mineral. 102, 777–794.
936 https://doi.org/10.2138/am-2017-5968
937 Park, J., Morgan, J.K., Zelt, C.A., Okubo, P.G., Peters, L., Benesh, N., 2007. Comparative velocity
938 structure of active Hawaiian volcanoes from 3-D onshore–offshore seismic tomography.
939 Earth Planet. Sci. Lett. 259, 500–516. https://doi.org/10.1016/j.epsl.2007.05.008
940 Pedregosa, F., Varoquaux, G., Gramfort, A., Michel, V., Thirion, B., Grisel, O., Blondel, M.,
941 Prettenhofer, P., Weiss, R., Dubourg, V., Vanderplas, J., Passos, A., Cournapeau, D., Brucher,
942 M., Perrot, M., Duchesnay, E., 2011. Scikit-learn: Machine Learning in Python. J. Mach.
943 Learn. Res. 12, 2825–2830.
944 Peterson, M.E., Kelley, K.A., Cottrell, E., Saal, A.E., Kurz, M.D., 2015. The Oxidation State of Fe in
945 Glasses from the Galapagos Archipelago: Variable Oxygen Fugacity as a Function of Mantle
946 Source. AGU Fall Abstr.
947 Peterson, M.E., Saal, A.E., Kurz, M.D., Hauri, E.H., Blusztajn, J.S., Harpp, K.S., Werner, R., Geist, D.J.,
948 2017. Submarine Basaltic Glasses from the Galapagos Archipelago: Determining the Volatile
949 Budget of the Mantle Plume. J. Petrol. 58, 1419–1450.
950 https://doi.org/10.1093/petrology/egx059

951 Pietruszka, A.J., Heaton, D.E., Marske, J.P., Garcia, M.O., 2015. Two magma bodies beneath the
952 summit of Kīlauea Volcano unveiled by isotopically distinct melt deliveries from the mantle.
953 Earth Planet. Sci. Lett. 413, 90–100. https://doi.org/10.1016/j.epsl.2014.12.040
954 Poland, M.P., Miklius, A., Montgomery-Brown, E.K., 2015. Magma supply, storage, and transport at
955 shield stage Hawaiian volcanoes, in: Characteristics of Hawaiian Volcanoes.
956 Putirka, K., 1999. Clinopyroxene + liquid equilibria to 100 kbar and 2450 K. Contrib. Mineral. Petrol.
957 135, 151–163. https://doi.org/10.1007/s004100050503
958 Putirka, K., 1997. Magma transport at Hawaii: Inferences based on igneous thermobarometry 4.
959 Putirka, K.D., 2008. Thermometers and Barometers for Volcanic Systems. Rev. Mineral. Geochem.
960 69, 61–120. https://doi.org/10.2138/rmg.2008.69.3
961 Roeder, P.L., Emslie, R.F., 1970. Olivine-liquid equilibrium. Contrib. Mineral. Petrol. 29, 275–289.
962 https://doi.org/10.1007/BF00371276
963 Shejwalkar, A., Coogan, L.A., 2013. Experimental calibration of the roles of temperature and
964 composition in the Ca-in-olivine geothermometer at 0.1MPa. Lithos 177, 54–60.
965 https://doi.org/10.1016/j.lithos.2013.06.013
966 Sides, I., Edmonds, M., Maclennan, J., Houghton, B.F., Swanson, D.A., Steele-MacInnis, M.J., 2014.
967 Magma mixing and high fountaining during the 1959 Kīlauea Iki eruption, Hawai'i. Earth
968 Planet. Sci. Lett. 400, 102–112. https://doi.org/10.1016/j.epsl.2014.05.024
969 Sobolev, A.V., Hofmann, A.W., Kuzmin, D.V., Yaxley, G.M., Arndt, N.T., Chung, S.-L., Danyushevsky,
970 L.V., Elliott, T., Frey, F.A., Garcia, M.O., Gurenko, A.A., Kamenetsky, V.S., Kerr, A.C.,
971 Krivolutskaya, N.A., Matvienkov, V.V., Nikogosian, I.K., Rocholl, A., Sigurdsson, I.A.,
972 Sushchevskaya, N.M., Teklay, M., 2007. The Amount of Recycled Crust in Sources of Mantle-
973 Derived Melts 316, 7.
974 Stock, M.J., Bagnardi, M., Neave, D.A., Maclennan, J., Bernard, B., Buisman, I., Gleeson, M.L.M.,
975 Geist, D., 2018. Integrated Petrological and Geophysical Constraints on Magma System
976 Architecture in the Western Galápagos Archipelago: Insights From Wolf Volcano. Geochem.
977 Geophys. Geosystems 19, 4722–4743. https://doi.org/10.1029/2018GC007936
978 Stock, M.J., Geist, D., Neave, D.A., Gleeson, M.L.M., Bernard, B., Howard, K.A., Buisman, I.,
979 Maclennan, J., 2020. Cryptic evolved melts beneath monotonous basaltic shield volcanoes in
980 the Galápagos Archipelago. Nat. Commun. 11, 3767. https://doi.org/10.1038/s41467-020-
981 17590-x
982 Sun, S. -s., McDonough, W.F., 1989. Chemical and isotopic systematics of oceanic basalts:
983 implications for mantle composition and processes. Geol. Soc. Lond. Spec. Publ. 42, 313–
984 345. https://doi.org/10.1144/GSL.SP.1989.042.01.19
985 Taracsák, Z., Hartley, M.E., Burgess, R., Edmonds, M., Iddon, F., Longpré, M.-A., 2019. High fluxes of
986 deep volatiles from ocean island volcanoes: Insights from El Hierro, Canary Islands. Geochim.
987 Cosmochim. Acta 258, 19–36. https://doi.org/10.1016/j.gca.2019.05.020
988 Thompson, R., 1987. Phase-equilibria constraints on the genesis and magmatic evolution of oceanic
989 basalts. Earth-Sci. Rev. 24, 161–210. https://doi.org/10.1016/0012-8252(87)90023-7
990 Thompson, R.N., Gibson, S.A., 2000. Transient high temperatures in mantle plume heads inferred
991 from magnesian olivines in Phanerozoic picrites. Nature 407, 502–506.
992 https://doi.org/10.1038/35035058
993 Vidito, C., Herzberg, C., Gazel, E., Geist, D., Harpp, K., 2013. Lithological structure of the Galápagos
994 Plume: Lithological Structure Galpagos Plume. Geochem. Geophys. Geosystems 14, 4214–
995 4240. https://doi.org/10.1002/ggge.20270
996 Vigouroux, N., Williams-Jones, G., Chadwick, W., Geist, D., Ruiz, A., Johnson, D., 2008. 4D gravity
997 changes associated with the 2005 eruption of Sierra Negra volcano, Galápagos. GEOPHYSICS
998 73, WA29–WA35. https://doi.org/10.1190/1.2987399
999 Villagómez, D.R., Toomey, D.R., Geist, D.J., Hooft, E.E.E., Solomon, S.C., 2014. Mantle flow and
1000 multistage melting beneath the Galápagos hotspot revealed by seismic imaging. Nat. Geosci.
1001 7, 151–156. https://doi.org/10.1038/ngeo2062

1002 Wager, L.R., Brown, G.M., Wadsworth, W.J., 1960. Types of Igneous Cumulates. J. Petrol. 1, 73–85.
1003 https://doi.org/10.1093/petrology/1.1.73
1004 Ward, J.H., 1963. Hierarchical Grouping to Optimize an Objective Function. J. Am. Stat. Assoc. 58,
1005 236–244. https://doi.org/10.1080/01621459.1963.10500845
1006 Welsch, B., Hammer, J., Hellebrand, E., 2014. Phosphorus zoning reveals dendritic architecture of
1007 olivine. Geology 42, 867–870. https://doi.org/10.1130/G35691.1
1008 White, W.M., McBirney, A.R., Duncan, R.A., 1993. Petrology and geochemistry of the Galápagos
1009 Islands: Portrait of a pathological mantle plume. J. Geophys. Res. Solid Earth 98, 19533–
1010 19563. https://doi.org/10.1029/93JB02018
1011 Wieser, P.E., Edmonds, M., Maclennan, J., Jenner, F.E., Kunz, B.E., 2019. Crystal scavenging from
1012 mush piles recorded by melt inclusions. Nat. Commun. 10, 5797.
1013 https://doi.org/10.1038/s41467-019-13518-2
1014 Wieser, P.E., Edmonds, M., Maclennan, J., Wheeler, J., 2020. Microstructural constraints on
1015 magmatic mushes under Kīlauea Volcano, Hawai'i. Nat. Commun. 11, 14.
1016 https://doi.org/10.1038/s41467-019-13635-y
1017 Winpenny, B., Maclennan, J., 2011. A Partial Record of Mixing of Mantle Melts Preserved in Icelandic
1018 Phenocrysts. J. Petrol. 52, 1791–1812. https://doi.org/10.1093/petrology/egr031
1019 Wood, B.J., Blundy, J.D., 1997. A predictive model for rare earth element partitioning between
1020 clinopyroxene and anhydrous silicate melt. Contrib. Mineral. Petrol. 129, 166–181.
1021 https://doi.org/10.1007/s004100050330
1022 Zanon, V., Pimentel, A., 2015. Spatio-temporal constraints on magma storage and ascent conditions
1023 in a transtensional tectonic setting: The case of the Terceira Island (Azores). Am. Mineral.
1024 100, 795–805. https://doi.org/10.2138/am-2015-4936
1025 Zanon, V., Pimentel, A., Auxerre, M., Marchini, G., Stuart, F.M., 2020. Unravelling the magma feeding
1026 system of a young basaltic oceanic volcano. Lithos 352–353, 105325.
1027 https://doi.org/10.1016/j.lithos.2019.105325
1028

This manuscript represents a post-print that has been accepted in the *Journal of Petrology* following peer-review (submitted 24th of August 2020).

# FIGURES

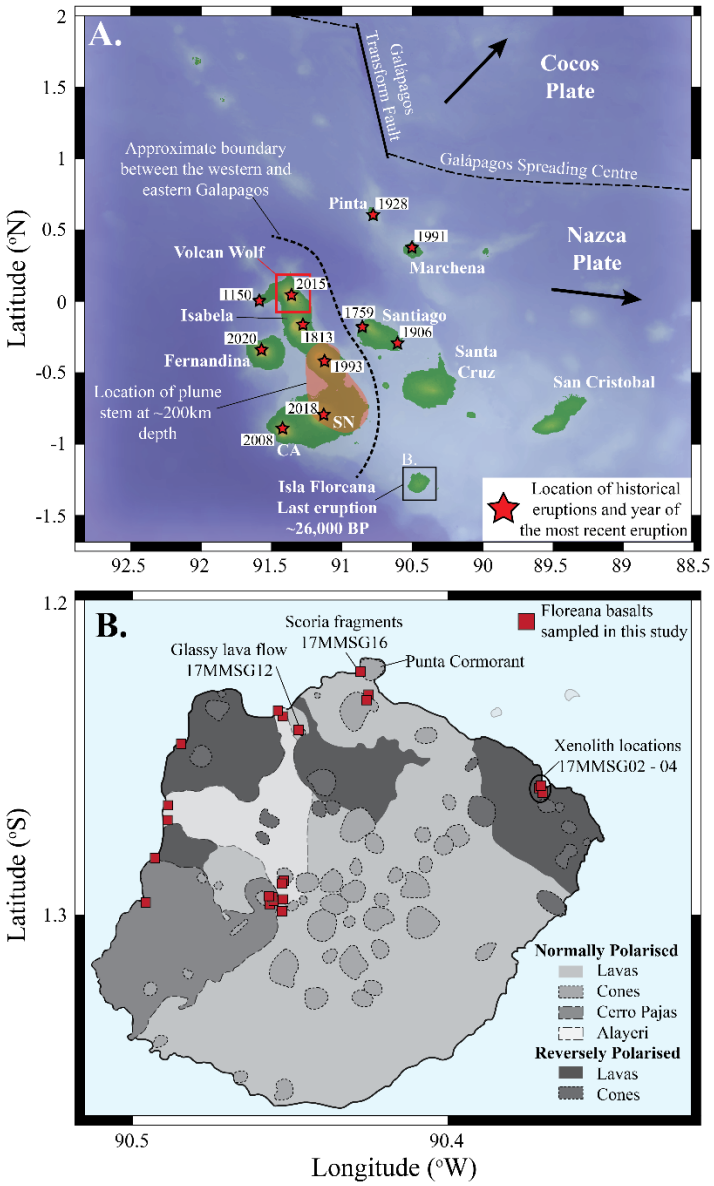


**Figure 1 - A.** Regional map of the Galápagos Archipelago highlighting the location of Isla Floreana, Cerro Azul (CA), Sierra Negra (SN) and Wolf volcanoes. Dates show the most recent eruptions at historically active volcanic centres. Black arrows show the direction of plate motion for the Nazca and Cocos tectonic plates. **B.** Geological map of Floreana adapted from Harpp et al. (2014a). Dashed lines delineate monogenetic scoria cones. Normally and reversely polarised lava flows are shown along with the largest (Cerro Pajas) and most recent (Alayeri; ~26,000 years) eruptions on the island.

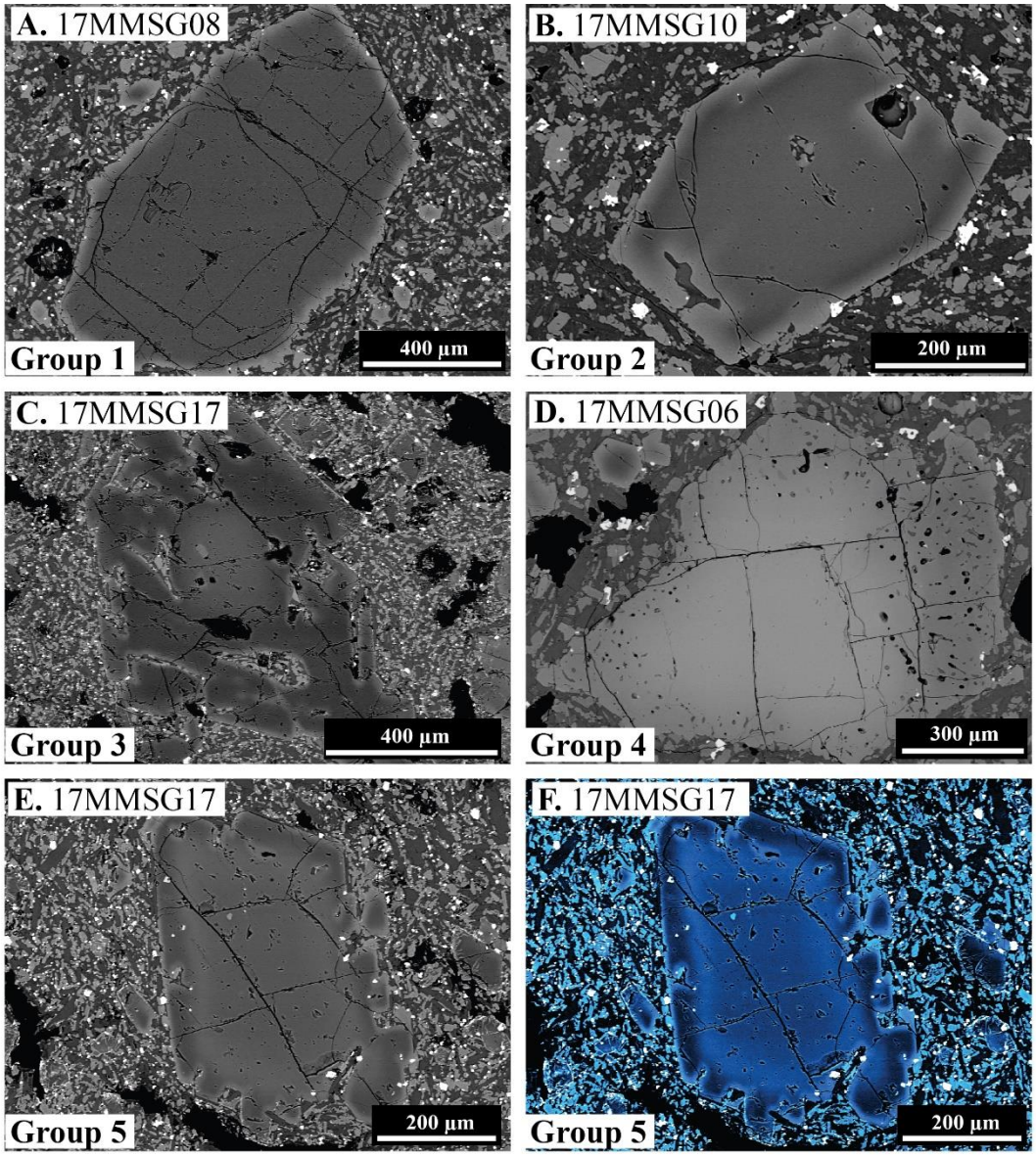


**Figure 2 –** Backscatter Electron images. **A.** Group 1 olivines – euhedral to subhedral crystal morphologies with large, unzoned, crystal cores and narrow, normally-zoned rims. **B.** Group 2 olivines – subhedral to euhedral crystals with clear, reverse-zoning profiles. **C.** Group 3 olivines – skeletal crystals with high forsterite overgrowths on low forsterite cores. **D.** Group 4 olivines – anhedral crystals with sieved textured, reverse zoned rims. **E.** (greyscale) and **F.** (false colour) Group 5 olivines – crystals preserve at least 4 composition zones over ~100-200 µm. False colour image (**F.**) is used to highlight the compositional zoning of the Group 5 olivine, with the intensity of the blue colour associated with the Fo composition of the crystal (darker = higher Fo).

This manuscript represents a post-print that has been accepted in the *Journal of Petrology* following peer-review (submitted 24th of August 2020).

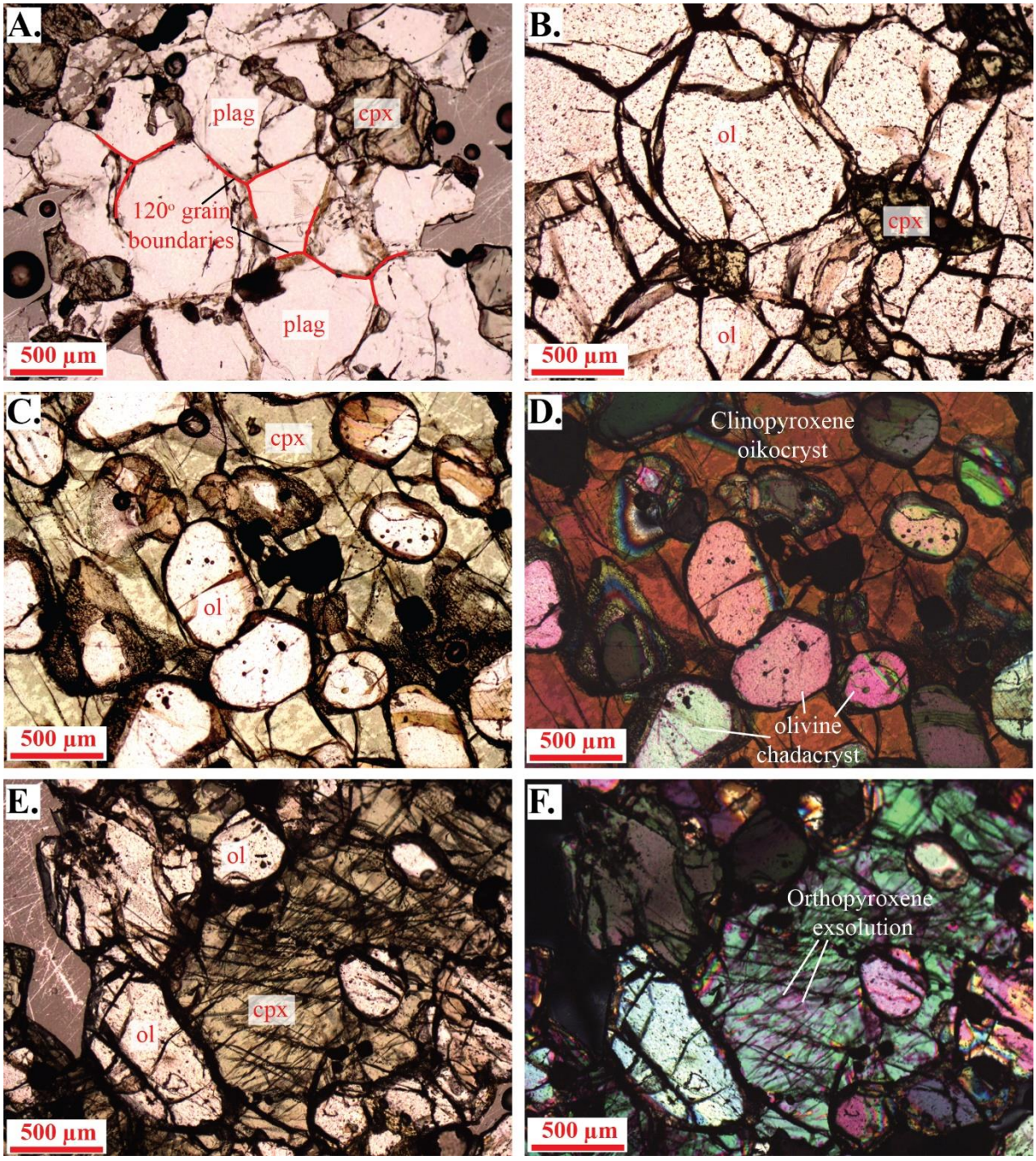


**Figure 3 -** Plane Polarised Light (**A. – C.** and **E.**) and Crossed Polarised Light (**D., F.**) images of Floreana xenoliths. **A.** – gabbroic xenolith (17MMSG04b), highlighting near 120° grain boundaries at monomineralic plagioclase (plag) triple junctions. **B.** – dunitic xenolith (17MMSG04c) with intercumulus clinopyroxene (cpx). **C.** and **D.** – wehrlitic xenolith (17MMSG02c) showing a large clinopyroxene oikocryst surrounding olivine (ol) chadacrysts. **E.** and **F.** – wehrlitic xenolith (sample 17MMSG03a) showing olivine chadacrysts within a clinopyroxene oikocryst. Orthopyroxene exsolution lamallae are visible within the clinopyroxene.

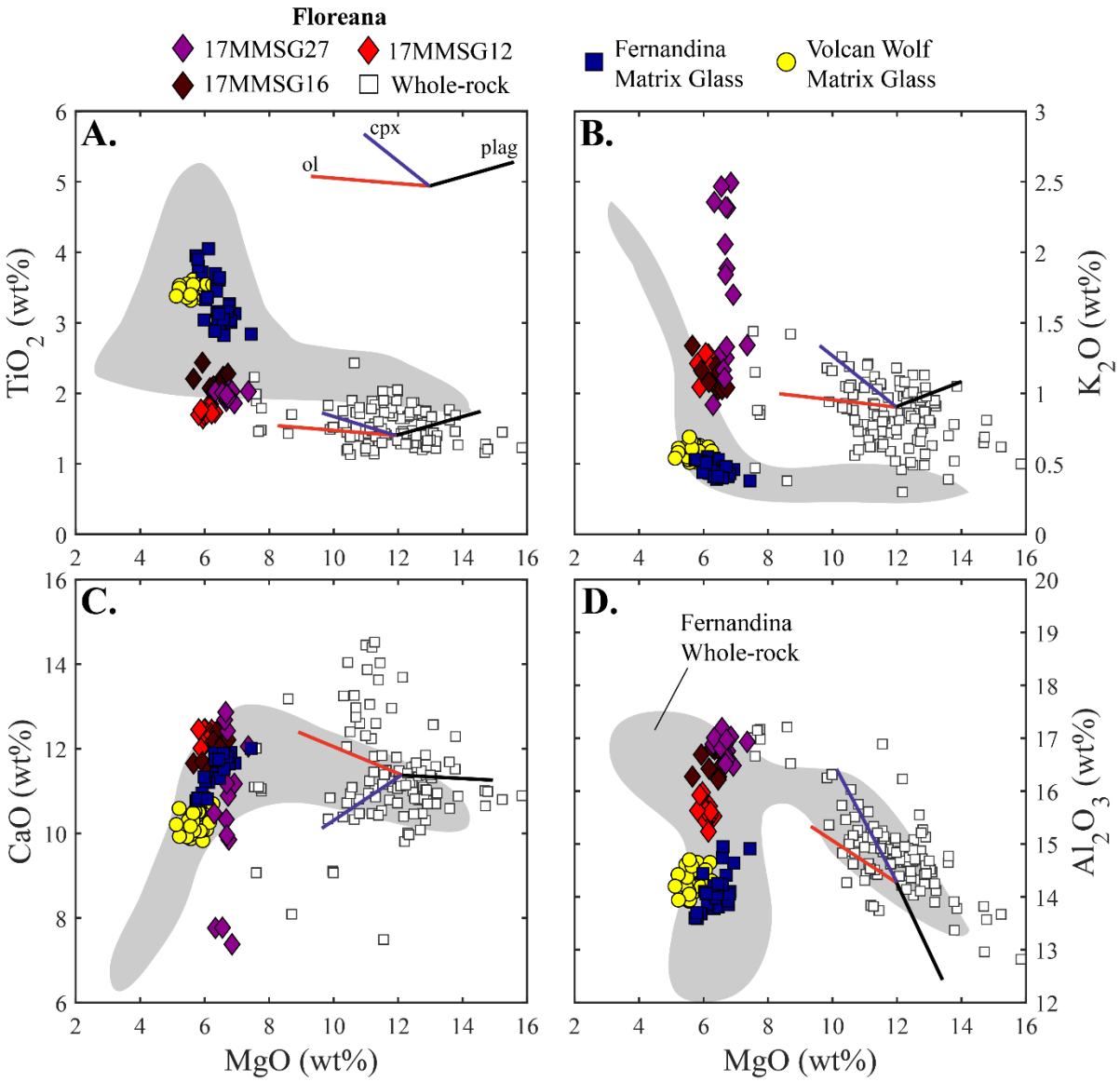


**Figure 4** – Major element compositions of matrix glasses (this study) and whole-rocks (Harpp et al., 2014a) from Floreana, as well as glasses from Fernandina (Peterson et al., 2017) and Wolf volcano (Stock et al., 2018) in the western Galápagos Archipelago. Lines show trajectories of liquid compositional evolution for olivine (ol; red), clinopyroxene (cpx; blue) and plagioclase (plag; black) crystallisation. The grey field shows whole-rock data from Isla Fernandina in the western Galápagos (Allan and Simkin, 2000; Geist et al., 2006). The 2σ precision of our matrix glass analyses is smaller than the symbol size.

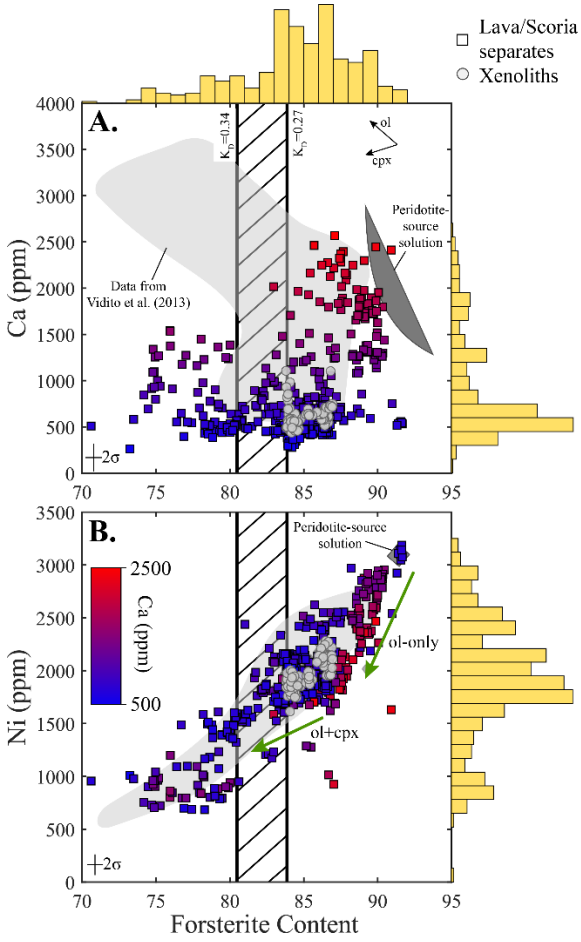


**Figure 5 –** Major and minor element compositions of olivine crystals from the Isla Floreana basalts. **A**. Fo vs. Ca and **B** Fo vs. Ni in Galápagos olivine crystals displaying analyses from our lava/scoria separates and xenolith samples, as well as a compilation of available olivine data from Floreana (Vidito et al. 2013). Our lava/scoria analyses are coloured according to their Ca concentration. The histograms above and to the right of the plots show the data distributions (excluding *in situ* analyses of xenolithic olivines). Peridotite source solutions are taken from Herzberg (2011) and Matzen et al. (2017a). Black arrows in **A.** show the trajectory of crystal compositional evolution during olivine (ol) and clinopyroxene (cpx) crystallisation (taken from Gleeson and Gibson, 2019). The green lines in **B.** show the trajectories of crystal compositional evolution during olivine only and olivine + clinopyroxene fractional crystallisation (from Gleeson and Gibson, 2019). The vertical black lines show the forsterite compositions of crystals calculated to be in equilibrium with the matrix glass composition of tephra sample 17MMSG16 ($K_d$ = 0.27 – 0.34 after Matzen et al. 2011, and Roeder and Emslie 1970).

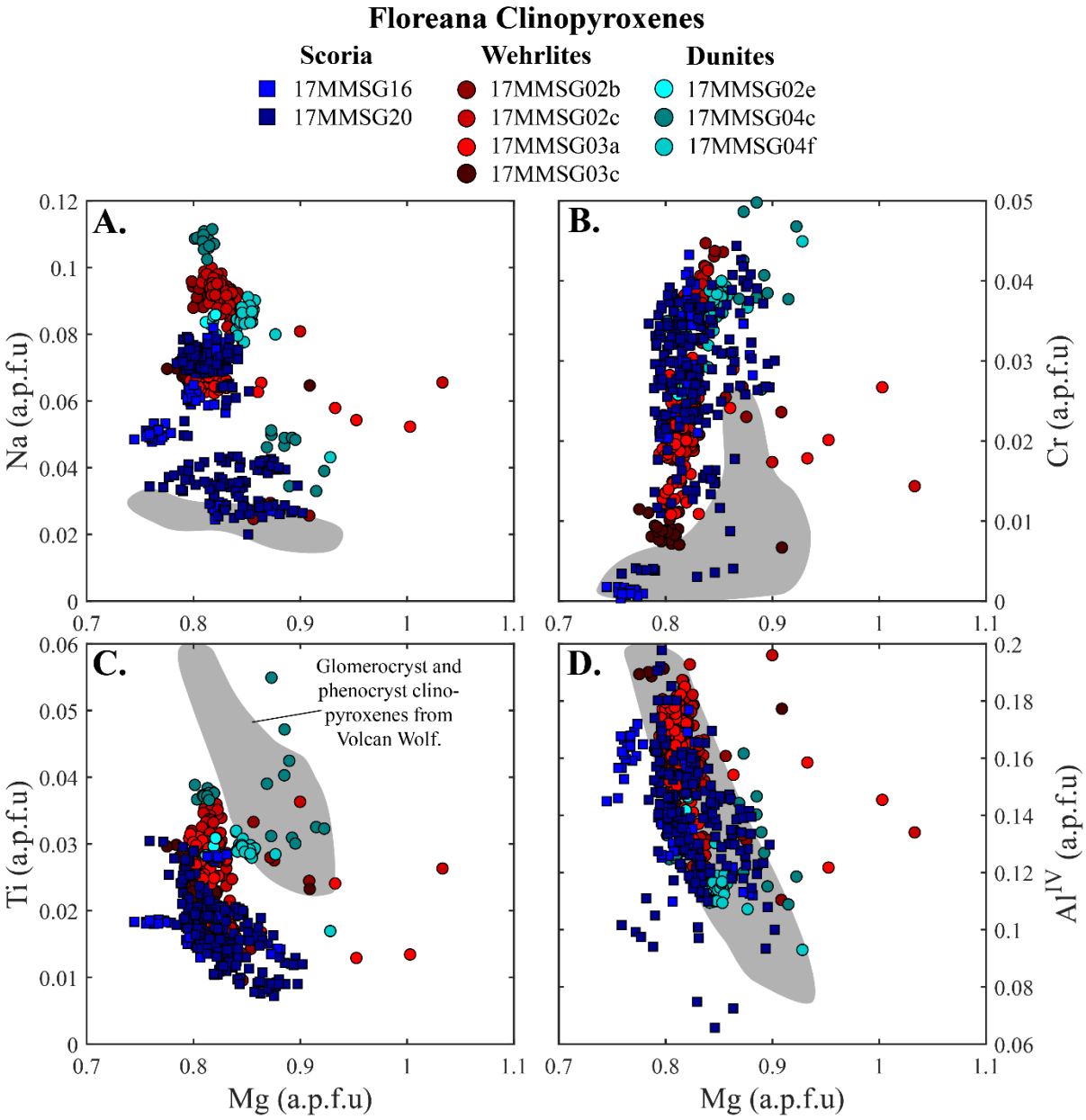


**Figure 6** – Major element composition of Floreana clinopyroxenes from our scoria, wehrlite and dunite samples. Data is shown as atoms per formula unit (a.p.f.u) on the basis of 6 oxygens. The grey field shows the compositions of clinopyroxenes from Wolf volcano in the western Galápagos Archipelago (from Stock et al. 2018). The 2σ precision of our clinopyroxene analyses is smaller than the symbol size.

This manuscript represents a post-print that has been accepted in the *Journal of Petrology* following peer-review (submitted 24th of August 2020).

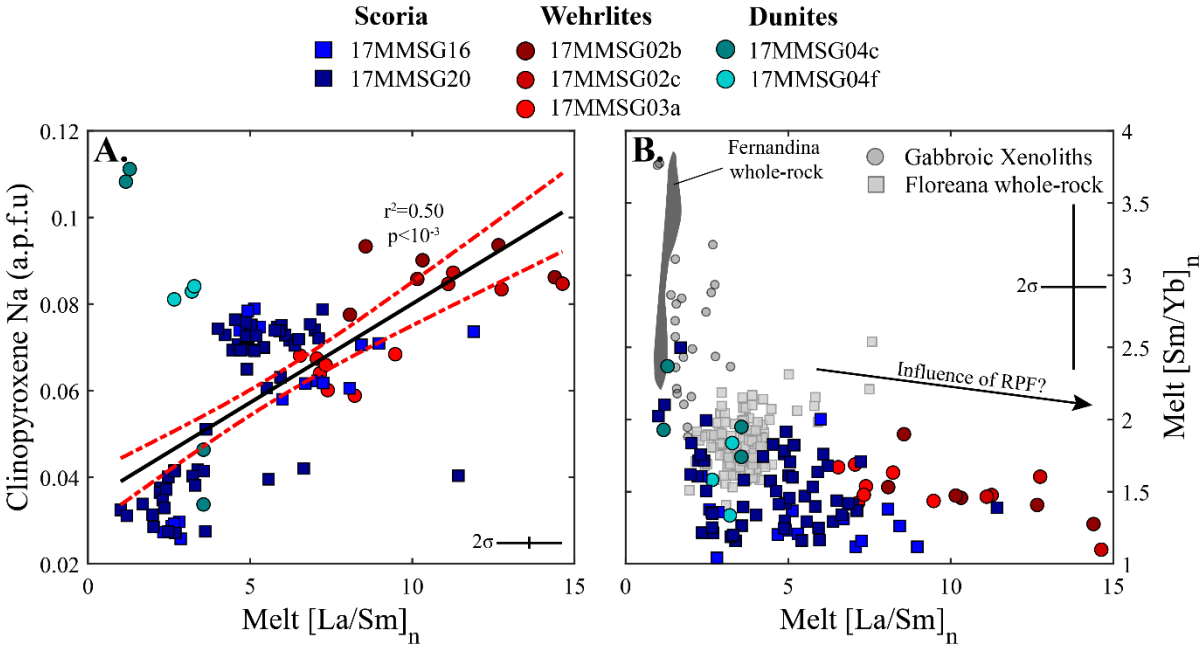


1082

1083 **Figure 7 –** Trace element composition of the Floreana clinopyroxenes and their relation to major
1084 element systematics. **A.** $[La/Sm]_n$ vs. Na in clinopyroxenes from our scoria samples and wehrlite and
1085 dunite xenoliths ($[La/Sm]_n$ is shown as the composition of melt in equilibrium with each
1086 clinopyroxene). The black line shows a regression through the data ($r^2 = 0.50$) and the red dashed
1087 lines show the 95% confidence limits on the regression. The correlation indicates that trace element
1088 enrichment in the Floreana clinopyroxenes is associated with anomalously high Na contents. **B.**
1089 $[La/Sm]_n$ vs. $[Sm/Yb]_n$ of melts calculated to be in equilibrium with our Floreana clinopyroxenes
1090 using the model of Wood and Blundy (1997). The black arrow shows the approximate trend of crystal
1091 compositional evolution hypothesised to occur as a result of clinopyroxene crystallisation during
1092 reactive porous flow within the cumulate mush (RPF). The grey field shows whole-rock compositions
1093 from Fernandina (Geist et al., 2006; White et al., 1993). **B.** additionally shows the whole-rock
1094 compositions of erupted Floreana lavas (Harpp et al., 2014a) and analyses of the gabbroic xenoliths
1095 from Floreana (this study). Error bars show the fully propagated 2σ precision of our analyses.

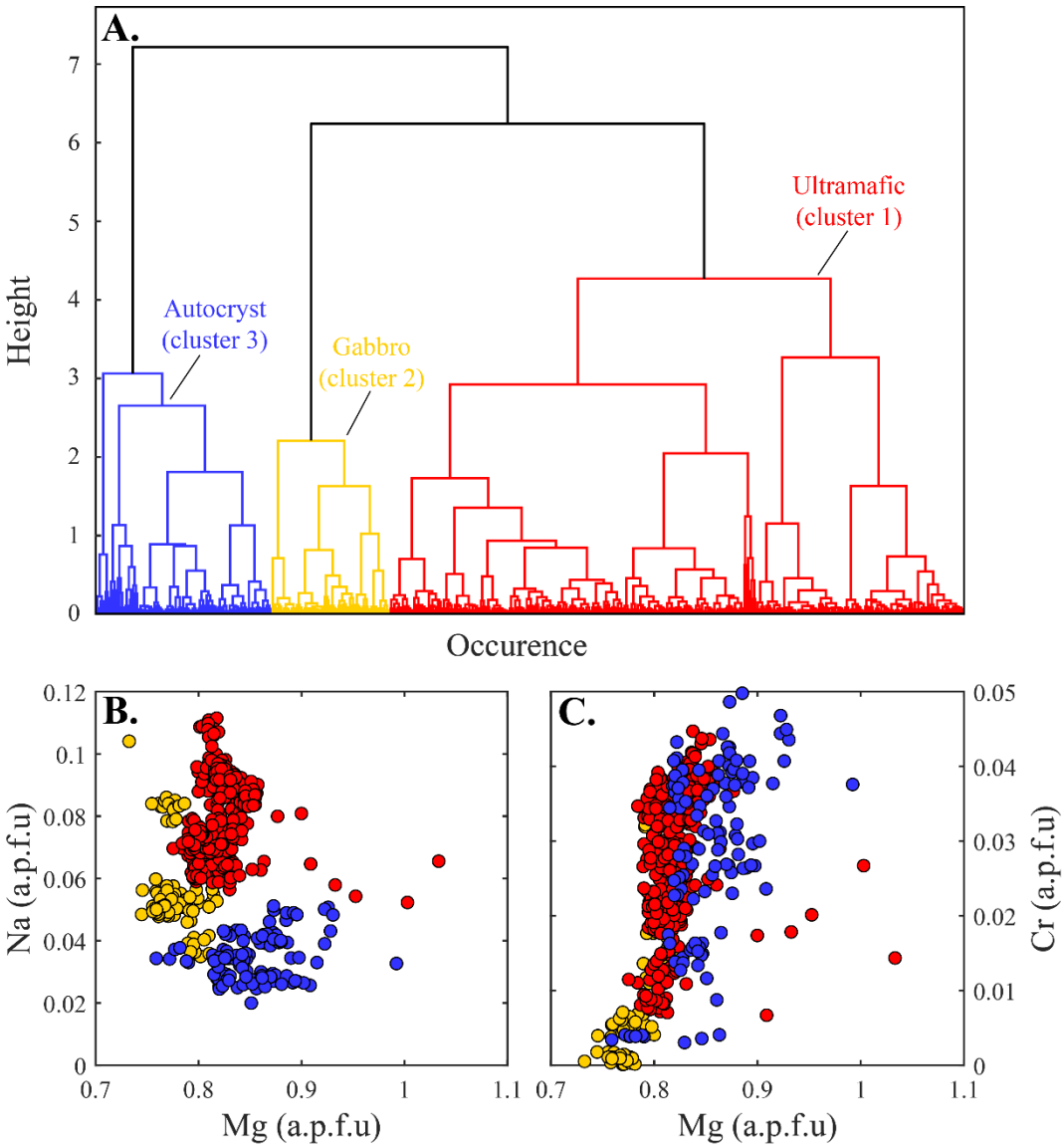


**Figure 8 – A.** Hierarchical cluster analysis of our clinopyroxene major element analyses. Cluster analysis was performed using Ward's method, which is built into the scikit-learn package in Python (Pedregosa et al., 2011; Ward, 1963). Height above the x-axis is a measure of the distance of separation of two clusters (i.e., the higher the join the more chemically distinct two clusters are). Colours show the high-level division of crystal compositions into three clusters: Cluster 1 is predominantly comprised of crystals from wehrlite and dunite xenoliths (red), Cluster 2 is composed of crystals from gabbroic xenoliths (yellow) and Cluster 3 (blue) is dominated by crystals separated from scoria samples. **B.** Na vs Mg and **C.** Cr vs Mg in our clinopyroxene analyses from the scoria and xenoliths, coloured by their cluster.

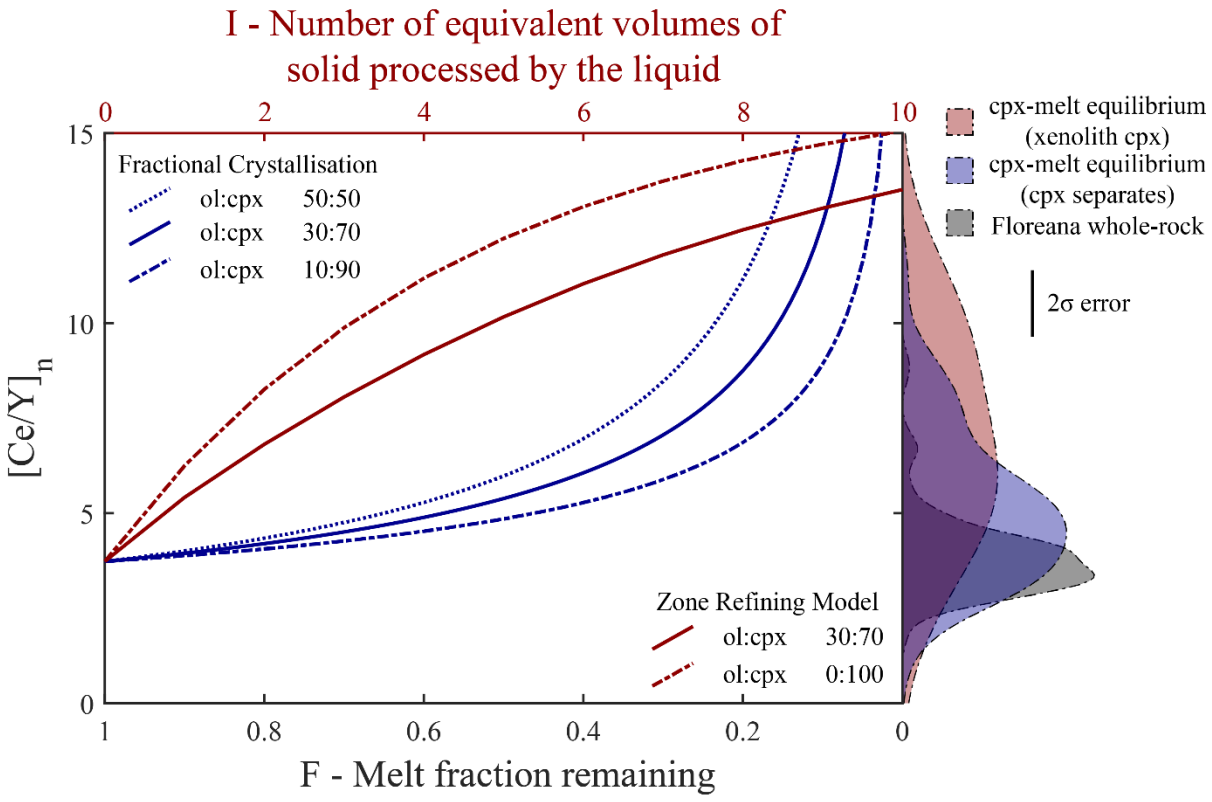


**Figure 9** – Models showing the evolution of melt $[Ce/Y]_n$ ratios as a function of the melt fraction remaining (F) during fractional crystallisation and as a function of the number of equivalent volumes of solid processed by the liquid (I) during reactive porous flow (red; using the zone-refining model of Harris, 1957). Line types show how models vary with different ratios of crystallising olivine (ol) and clinopyroxene (cpx). The kernel density plots show the $[Ce/Y]_n$ density distributions of liquids calculated to be in equilibrium with clinopyroxene crystals in our wehrlite and dunite xenoliths (red), scoria samples (blue; 2σ error for the clinopyroxene analyses is shown by the black bar), and whole-rock analyses of erupted Floreana basalts (grey; Harpp et al., 2014a). Clinopyroxene partition coefficients were calculated using the method of Wood and Blundy (1997), the mean major element composition of the Cluster 3 clinopyroxenes from this study, a temperature of 1225°C, and a pressure of 700 MPa. Initial Ce and Y concentrations for both models were taken as the mean values from the whole-rock dataset of Harpp et al. (2014a). Calculation increments are 0.01 in F and 0.1 in I.

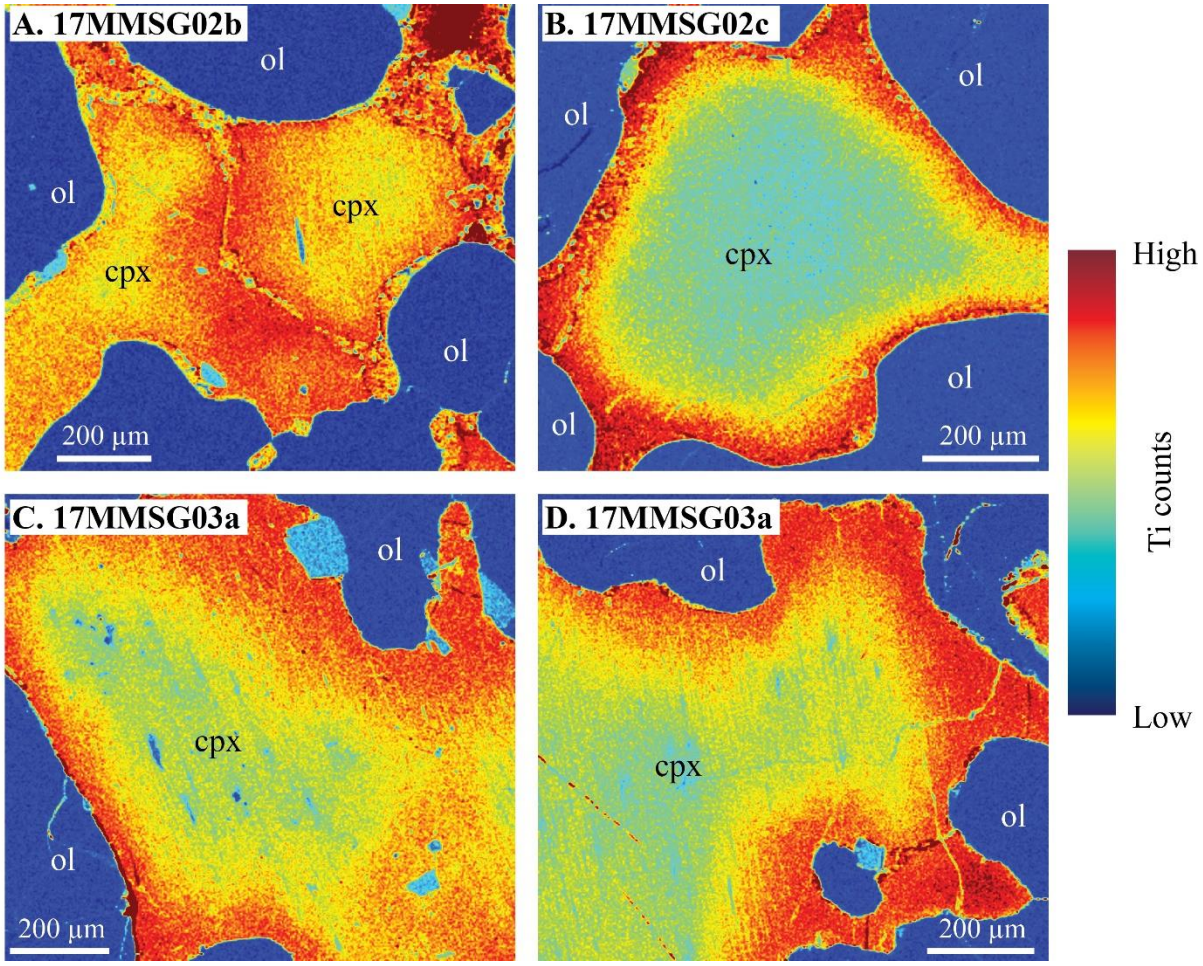


**Figure 10** – WDS maps of Ti counts in key clinopyroxene crystals from the Floreana wehrlite xenoliths. These maps display clear zoning in the xenolithic clinopyroxenes with Ti-poor cores and Ti-rich rims. EPMA transects across some of the wehrlitic clinopyroxenes indicates that the Ti concentrations in these crystals may vary from ~0.6 wt% to ~1.3 wt% $TiO_2$ (see Supplementary Information). The dark blue regions surrounding clinopyroxene grains are olivine crystals.

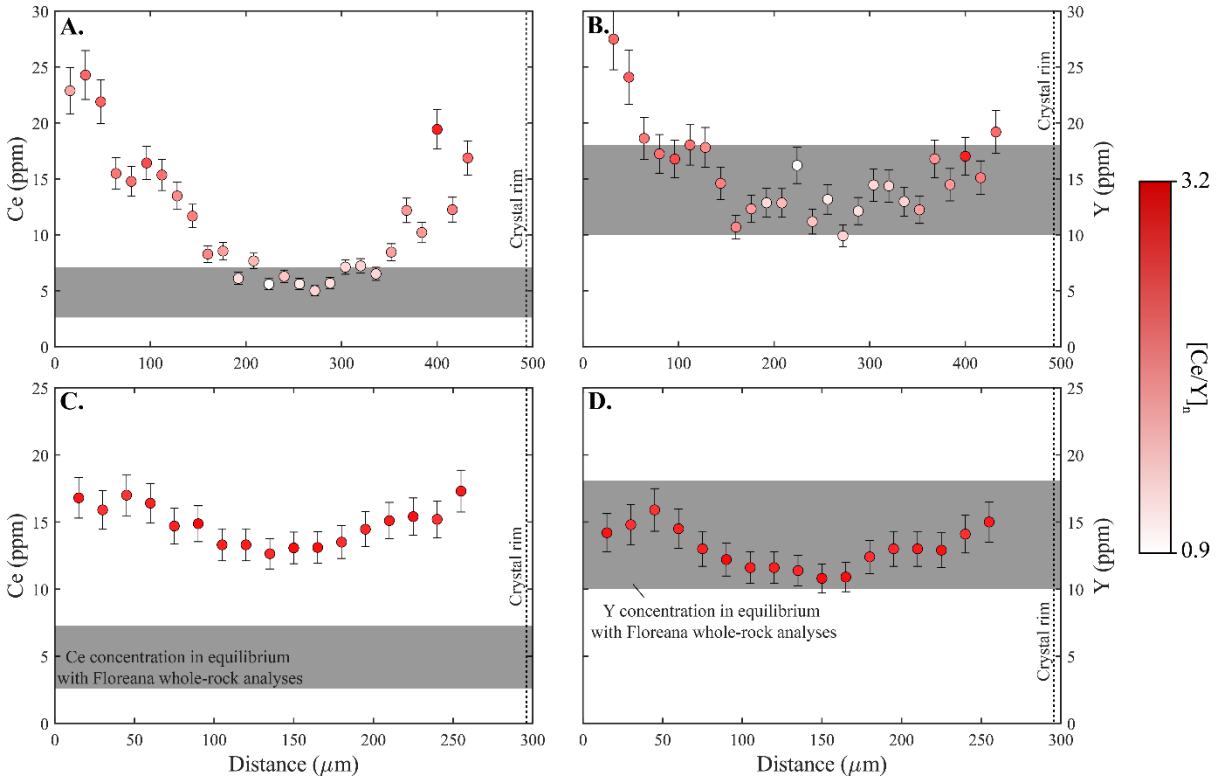


**Figure 11 –** LA-ICP-MS transects showing Ce (**A, C**) and Y (**B, D**) zoning across two clinopyroxene grains in a wehrlitic xenolith (17MMSG02c). **A.** and **B.** show a transect across the core of a large clinopyroxene oikocryst. **C.** and **D.** show a transect across the apparent core of a smaller clinopyroxene oikocryst. Points are coloured according to their $[Ce/Y]_n$ ratio (see colour scale). The grey bars show the crystal compositions calculated to be in equilibrium with whole-rock analyses of erupted Floreana basalts (Harpp et al., 2014a).

This manuscript represents a post-print that has been accepted in the *Journal of Petrology* following peer-review (submitted 24th of August 2020).

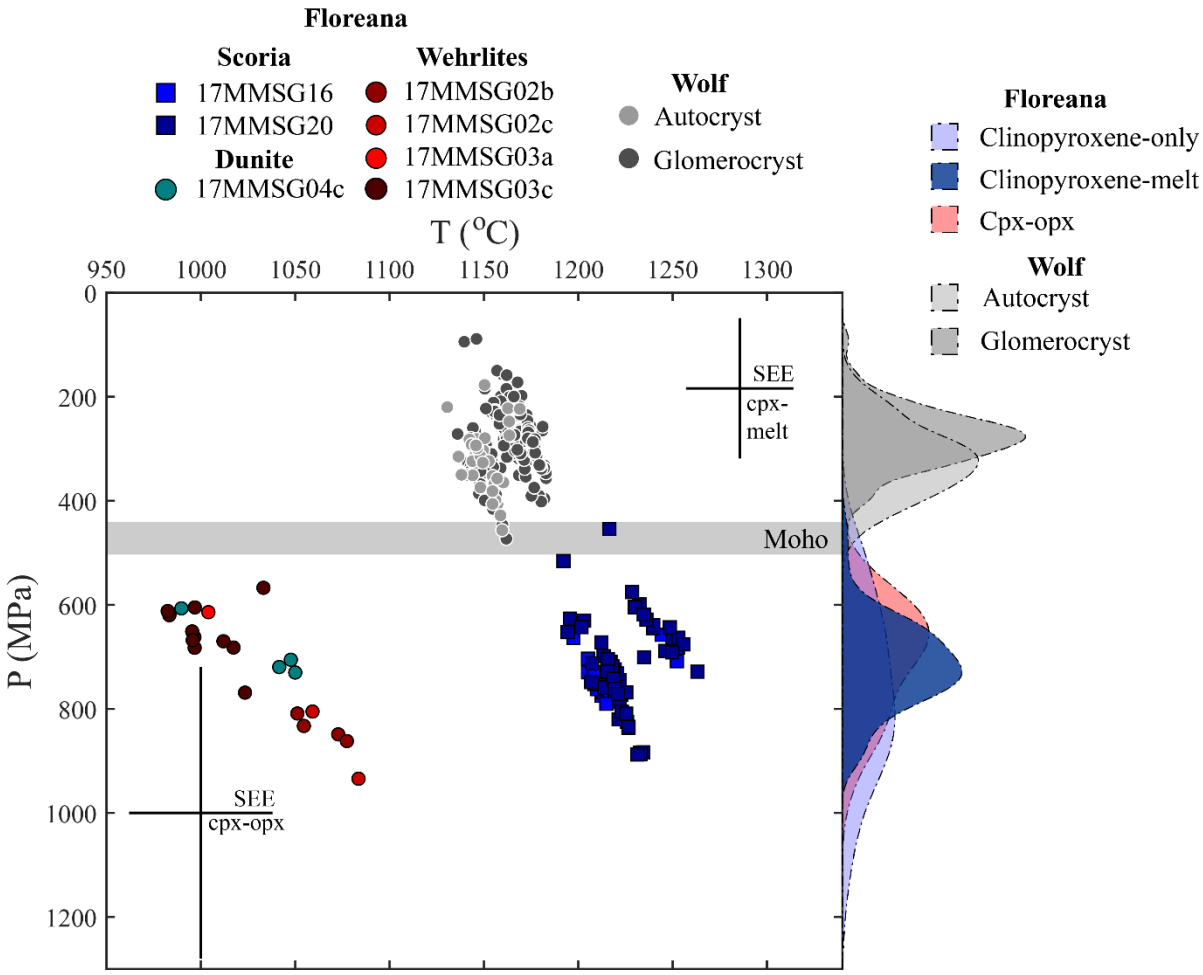


**Figure 12 –** Petrological thermobarometry results. The kernel density plots to the right show the density distributions of barometric results from different models (light blue – clinopyroxene-only, Putirka (2008); dark blue – clinopyroxene-melt, Neave and Putirka (2017); red – clinopyroxene-orthopyroxene Putirka (2008)). The grey bar shows the Moho depth beneath Fernandina (from Feighner and Richards, 1994) and the grey points and kernel density estimates show clinopyroxene-melt thermobarometric results for autocrysts and glomerocrysts from Wolf volcano (from Stock et al., 2018). The Standard Estimated Error (SEE) of the clinopyroxene-melt and orthopyroxene-clinopyroxene thermobarometers are given.

This manuscript represents a post-print that has been accepted in the *Journal of Petrology* following peer-review (submitted 24th of August 2020).

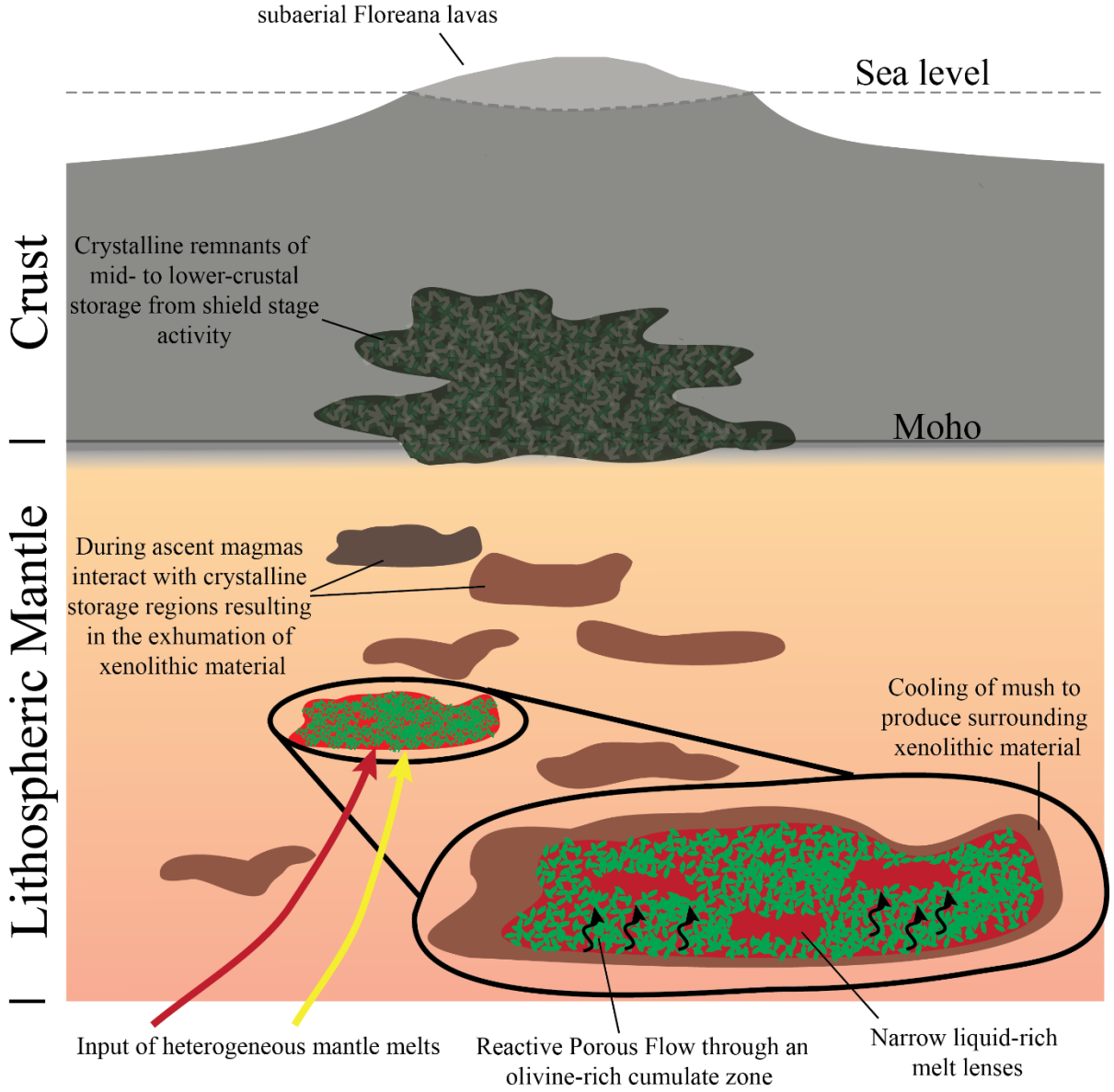


**Figure 13** – Schematic illustration of the magma plumbing system beneath Floreana. No magma storage is identified within the crust. Instead, our barometric results indicate that Floreana magmas ascend directly from the upper mantle, where they are stored at a depth of ~23.7 ±5.1 km. Floreana magma storage regions are dominated by crystal-rich domains (i.e. mush). Reactive porous flow is identified as an important mechanism of melt migration and magma differentiation in the crystal-rich storage regions, although our results shows that some crystallisation occurs within liquid-rich domains.

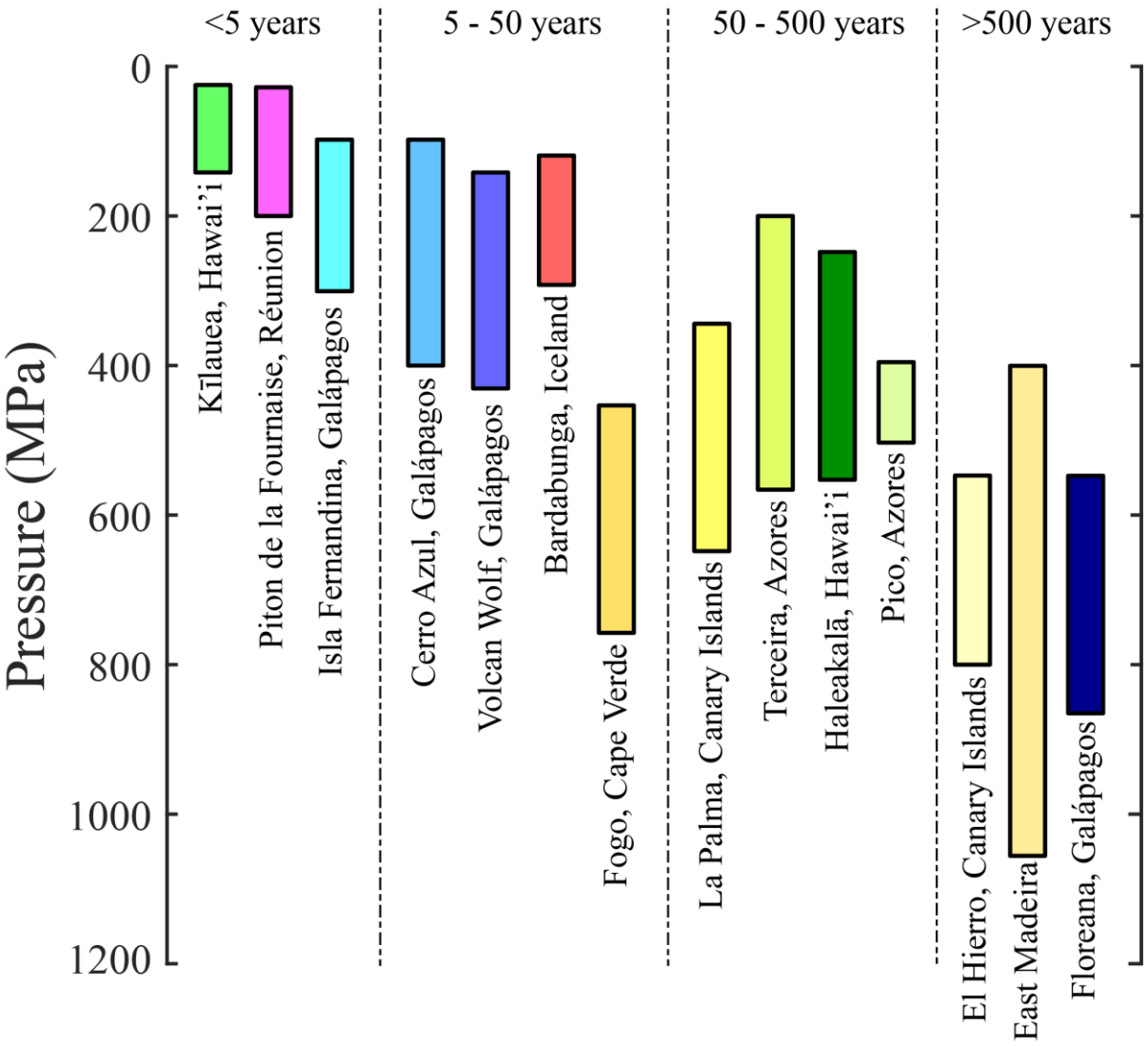


**Figure 14 -** Compilation of barometric estimates for the primary magma storage region beneath various ocean island volcanoes worldwide. Data is divided according to the approximate repose period between eruptions at each volcano (estimated using data from Global Volcanism Program, 2013), which is used as a proxy for the flux of magma entering the lithosphere. A general trend to greater magma storage pressures is observed with increasing repose period, indicating that the flux of magma from the mantle has a first order control on the depth of magma storage. Data from (Famin et al., 2009; Geist et al., 1998; Hammer et al., 2016; Hartley et al., 2018; Klügel et al., 2015; Poland et al., 2015; Stock et al., 2018; Zanon et al., 2020; Zanon and Pimentel, 2015).